Late Quaternary slip-rates along the Moxi and Zheduotang segments of the SE Xianshuihe fault, eastern Tibet, and geodynamic implications

Mingkun Bai[1,2], Marie-Luce Chevalier[1,3*], Shiguang Wang[1,6], Jiawei Pan[1,3], Philippe Hervé Leloup[4], Anne Replumaz[5], Kaiyu Li[1], Qiong Wu[1,6], Fucai Liu[1,6], Haibing Li[1,3], Jinjiang Zhang[2]

[1] Key Laboratory of Deep-Earth Dynamics of Ministry of Natural Resources, Institute of Geology, Chinese Academy of Geological Sciences, 26 Baiwanzhuang Rd, Beijing 100037, People's Republic of China

[2] Ministry of Education Key Laboratory of Orogenic Belts and Crustal Evolution, School of Earth and Space Sciences, Peking University, Beijing 100871, People's Republic of China

[3] Southern Marine Science and Engineering Guangdong Laboratory (Guangzhou), Guangzhou 511458, People's Republic of China

[4] Laboratoire de géologie de Lyon, CNRS UMR 5570, Université de Lyon, Villeurbanne, France

[5] ISTerre, Université Grenoble Alpes, CNRS, Grenoble, France

[6] School of Earth Sciences and Resources, China University of Geosciences, Beijing, 29 Xueyuan Rd, Beijing 100083, China

Highlights

-The Zheduotang and Moxi fault slip-rates are 4.5(+0.9/-0.8) and 12.5(+2.3/-2.1) mm/yr, respectively

-The slip-rate increases towards the SE along the Xianshuihe fault system until at least Moxi

-Earthquake hazard is high in the Kangding region of the SE Xianshuihe fault

Abstract

[*]Corresponding author : Marie-Luce Chevalier (mlchevalier@hotmail.com), Tel: +86 13466654223

The Xianshuihe fault in eastern Tibet is one of the most active faults in China, with the next large earthquake most likely to occur along its SE part near Kangding. Quantifying its slip rate along the three parallel branches (Yalahe, Selaha and Zheduotang) as well as along the Moxi fault is essential to evaluate regional earthquake hazard, necessary to the construction of the Chengdu-Lhasa railroad. Here, we expand our previous work on the Selaha fault to the Zheduotang and Moxi faults, with observations on the Yalahe fault and the newly discovered Mugecuo South fault zone. Using tectonic-geomorphology approaches (LiDAR, UAV and ^{10}Be dating), we had determined late Quaternary slip rates of 9.75±0.15 and 4.4±0.5 mm/yr along the NW and SE Selaha fault, respectively, hence had inferred a ~5 mm/yr rate along the parallel Zheduotang fault. Here, using the same methods, we confirm such rate (4.5[+0.9/-0.8] mm/yr, ZDT moraine site) thus suggest a total slip rate of >8.9±1.4 mm/yr in the SE Xianshuihe fault. Our rate along the Moxi fault (12.5[+2.3/-2.1] mm/yr, MX moraine site) is higher than those along the Ganzi (6-8 mm/yr) and Xianshuihe (~10 mm/yr) faults farther NW, which reinforces our earlier finding of a southeastward slip rate increase, in agreement with the eastward decrease of GPS vector values (with respect to Eurasia) located north of the fault. Our study reveals a high regional earthquake hazard (Mw6.5 to 7.3) in the near future, which adds to the challenge of building the new railroad in such mountainous area.

Plain Language Summary

The left-lateral Xianshuihe fault in eastern Tibet is one of the most active faults in China, with the next large earthquake most likely to occur along its SE part near Kangding city. Studying its activity and slip rate is essential to evaluate regional earthquake hazard, especially because it crosses Kangding city and because of the construction of the Chengdu-Lhasa railroad. Here, we expand our previous work on the Selaha fault to the Zheduotang and Moxi faults, together with key observations on the Yalahe fault and the newly discovered Mugecuo South fault zone. We find that the rate over the last ~100,000 years increases southeastwards along the Xianshuihe fault system, in

agreement with the eastward decrease of GPS vector values (with respect to Eurasia) located north of the fault. The fast slip rates and their complex spatial distribution in the Kangding region reveal a high earthquake hazard (Mw6.5 to 7.3) in the near future, which adds to the challenge of building the Chengdu- Lhasa railroad in such mountainous area.

1. Introduction

The eastern margin of the Tibetan Plateau is an important, active, tectonic boundary with numerous active faults which can accommodate slip due to the eastward motion of the plateau, as well as shortening with respect to the less deformed Sichuan Basin to its east (e.g., Molnar and Tapponnier, 1975; Tapponnier and Molnar, 1977; Wang et al., 1998; Wang and Burchfiel, 2000; Tapponnier et al., 2001) (Fig. 1). Eastern Tibet belongs to the “eastern Tibet seismic belt” or “N-S tectonic zone” (Deng et al., 2003; Zhang, 2013) along which an extremely large number of M>7 earthquakes occurred in history, particularly along the NW-striking, ~1400 km-long Xianshuihe (hereafter XSH) fault system, which consists of the Yushu/Batang, Ganzi, Xianshuihe and Moxi fault segments from NW to SE (e.g., Allen et al., 1991, Fig. 1): 16 M>7 and 26 M>6.5 earthquakes have ruptured almost its entire length since 1700, with three M>7.3 earthquakes along just the Xianshuihe fault segment since 1923 (Allen et al., 1991; Wen, 2000) (Fig. 2A). It has been suggested that following the 2008 Mw7.9 Wenchuan and 2013 Ms7 Lushan earthquakes, the seismic risk near Kangding increased by a factor of two (e.g., Parsons et al., 2008; Toda et al., 2008; Shan et al., 2013; Yang et al., 2015). The energy accumulated has since only partly been released by the 2014 Kangding earthquake sequence (Mw5.9 and 5.6) along the Selaha and NW Zheduotang faults near Kangding (Fig. 2A), with a remaining seismic gap that has not been filled since the 1955 Mw7.5 Kangding earthquake which occurred on the Zheduotang fault (Jiang et al., 2015a; Xie et al., 2017). Indeed, Bai et al. (2018), using their slip rate on the Selaha fault (~10 mm/yr) at a ~20 ka timescale, and moment accumulation rate since the 1955 Kangding earthquake, suggested that a M6.5 to 6.8 earthquake may strike the Kangding region in the near future. An increasing body of

evidence from geophysical and geological studies suggests that the Kangding region is the most dangerous section of the entire XSH fault (e.g., Allen et al., 1991; Jiang et al., 2015a; NSPRC, 2016; Shao et al., 2016; Wang and Shen, 2020), which would be tragic not only due to infrastructure damages but also because of landslides and mud flows due to the very steep slopes surrounding this large city (population = ~150,000).

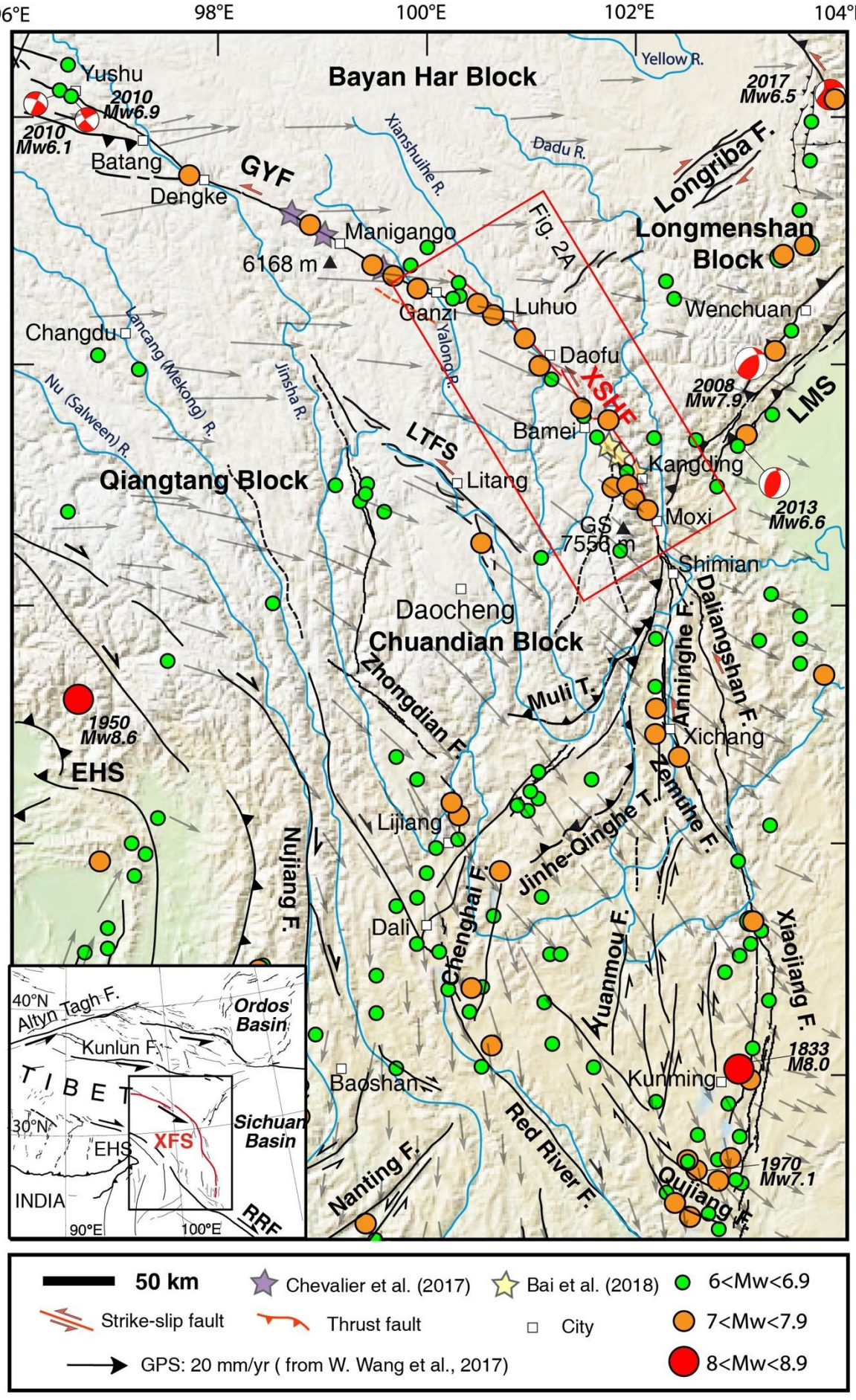
96°E
98°E
100°E
102°E
104°E
33°N
31°N
29°N
27°N
25°N
Bayan Har Block
Yushu
2010 Mw6.9
2010 Mw6.1
Batang
Dengke
GYF
Manigango
6168 m
Ganzi
Luhuo
Yellow R.
2017 Mw6.5
Xianshuihe R.
Dadu R.
Longriba F.
Longmenshan Block
Fig. 2A
Wenchuan
Changdu
Lancang (Mekong) R.
Nu (Salween) R.
Jinsha R.
Yalong R.
Daofu
JFSX
2008 Mw7.9
LMS
Bamei
LTFS
Litang
Kangding
Moxi
GS 7556 m
2013 Mw6.6
Qiangtang Block
Shimian
Daocheng
Chuandian Block
Daliangshan F.
Anninghe F.
Muli T.
Zhongdian F.
Xichang
1950 Mw8.6
EHS
Zemuhe F.
Lijiang
Jinhe-Qinghe T.
Nujiang F.
Chenghai F.
Dali
Xiaojiang F.
Xuanmou F.
1833 M8.0
Kunming
Baoshan
Red River F.
Nanting F.
1970 Mw7.1
Qujiang F.
40°N
Altyn Tagh F.
Ordos Basin
Kunlun F.
TIBET
30°N
EHS
XFS
Sichuan Basin
INDIA
90°E
100°E
RRF
50 km
Chevalier et al. (2017)
Bai et al. (2018)
6<Mw<6.9
Strike-slip fault
Thrust fault
City
7<Mw<7.9
GPS: 20 mm/yr (from W. Wang et al., 2017)
8<Mw<8.9

Figure 1: *The Xianshuihe fault system (XFS) in the frame of the India–Asia collision zone: Tectonic map of SE Tibet with digital elevation model (DEM) in the background. Horizontal GPS velocity field with respect to the stable Eurasian plate (W. Wang et al., 2017), focal mechanisms of instrumental earthquakes with Mw>6 (CMT catalog 1976–2019) (2008 Wenchuan, 2010 Yushu, 2013 Lushan and 2017 Jiuzhaigou), as well as earthquakes from USGS and CEA (1995), main peaks, cities, active faults (those of the Xianshuihe fault in red), tectonic blocks and rivers. LMS=Longmenshan, GYF= Ganzi-Yushu fault, XSHF=Xianshuihe fault, LTFS=Litang fault system, GS=Gongga Shan. Inset shows the Xianshuihe fault system (XFS) within Asia, EHS=Eastern Himalayan syntaxis, RRF=Red River fault.*

In order to better understand continental tectonics and assess regional seismic hazard in this particularly active region of eastern Tibet, precisely constraining the active fault slip-rates is essential. As slip-rates may vary temporally and/or spatially along a particular fault (e.g., Friedrich et al., 2003; Chevalier et al., 2005), it is important to estimate them at various timescales from a few tens of years (using geodetic techniques such as GPS or InSAR), to a few tens of ka (using tectonic-geomorphology approaches), to a few Ma (using geologic tools). Our previous work on the XSH fault system allowed us to suggest a southeastward increase of the late Quaternary slip rates between the Ganzi fault (~6-8 mm/yr, Chevalier et al., 2017) and XSH fault (~10 mm/yr, Bai et al., 2018) (Fig. 1), using tectonic-geomorphology approaches (^{10}Be cosmogenic dating of offset geomorphic surfaces). Bai et al. (2018) suggested that this increase may be due to the presence of the NE-striking, reverse/dextral Longriba fault system to the north, which marks the limit between the fast-moving Bayan Har block to the NW and the slow-moving Longmenshan block to the SE, as observed by GPS data (e.g., Gan et al., 2007; W. Wang et al. 2017, 2020; Y. Wang et al., 2017), hence resulting in faster slip-rate along the XSH fault compared to that on the Ganzi fault (Fig. 1). Such a SE increase of slip rate along the Xianshuihe fault system has also been documented using GPS data (Zhang, 2013; W. Wang et al., 2017, 2020; Y. Wang et al., 2017). However, at the longer-term timescale, the rate seems spatially constant at 7±1 mm/yr since the fault initiation at ~9 Ma (Zhang et al., 2017; Bai et al., 2018).

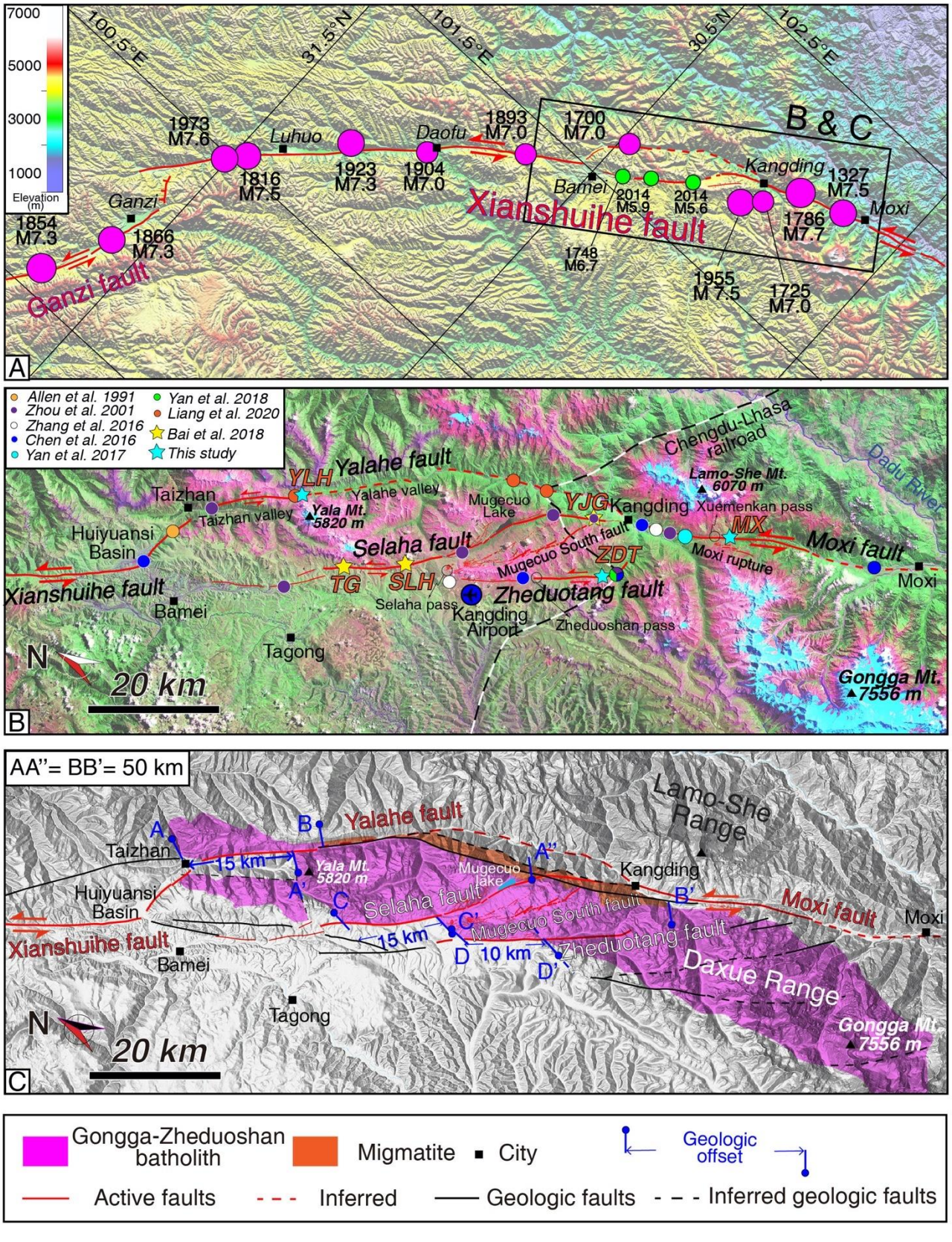

112

113 ***Figure 2:*** *The Xianshuihe fault. (A) Post 1700 A.D. earthquakes distribution (+ the 1327*
114 *earthquake) (e.g., USGS, Wen et al., 2008; Cheng et al., 2011) along the Xianshuihe and SE Ganzi*
115 *faults. (B) Landsat satellite image of the SE Xianshuihe fault (box in A), where the main trace of the*
116 *active Xianshuihe fault splays into the Yalahe, Selaha and Zheduotang faults before reconnecting as*

the Moxi fault farther to the SE. Location of main geographic and topographic features indicated, in addition to approximate location of study sites from others. (C) Simplified geologic map of the SE segment of the Xianshuihe fault, with the Gongga-Zheduoshan batholith and its geologic offsets (following Liu et al., 1977; Chen et al., 1985).

Near Kangding, the main, linear, XSH fault splits in the SE into three parallel segments: Yalahe, Selaha and Zheduotang (Fig. 2B). Following Bai et al. (2018) who determined the Selaha fault's late Quaternary horizontal slip-rate at three locations, in this paper, we constrain that of the other fault segments in the SE XSH fault near Kangding: the Zheduotang and Moxi faults, respectively located NW and SE of Kangding city. We use the same approach as in Bai et al. (2018) and study two moraine sites to 1) assess Bai et al. (2018)'s rate hypothesis along the Zheduotang segment and 2) assess whether the rate keeps increasing toward the SE along the Moxi segment. We also present preliminary observations on the activity of the central Yalahe fault, as well as of that of the newly discovered 'Mugecuo South' fault zone located between the Selaha and Zheduotang faults, on the NE slopes of the Zheduoshan Range. Finally, we discuss the rates distribution in the SE XSH fault in the framework of eastern Tibet, and assess regional seismic hazard. Our work also provides valuable data to the highly challenging Chengdu-Lhasa railroad construction, with 80% of this route underground, crossing all fault segments near Kangding (Fig. 2B).

2. Geological setting

The XSH fault system consists of a series of left-lateral strike-slip faults located in eastern Tibet, which separate the Bayan Har and Qiangtang/Chuandian blocks to the NE and SW, respectively (Fig. 1). It can be divided into four main segments: the Yushu/Batang fault at the NW end (where the 2010 Mw6.9 Yushu earthquake occurred), the Ganzi fault in the NW, the XSH and Moxi faults in the center, and the Anninghe-Zemuhe-Xiaojiang faults in the SE (Fig. 1). The active XSH fault has a single, linear, trace in the NW but splits into three right-stepping en-echelon segments towards the SE near Kangding: the Yalahe, Selaha and Zheduotang faults (Fig. 2B). These

active faults more or less follow geological faults that left-laterally offset the Gongga-Zheduoshan granite batholith (Chen et al., 1985) (Fig. 2C) and may be connected at depth (e.g., Allen et al., 1991; Jiang et al., 2015a; Li et al., 2020). While the Selaha and Zheduotang faults show evidence of recent activity along most of their traces, with numerous clear scarps, sag ponds, and left-lateral (with minor vertical) offsets of mostly moraines and gullies, such clear evidence are lacking along the Yalahe fault where parallel to the Selaha fault (Allen et al., 1991; Bai et al., 2018). This led Zhang et al. (2017) to suggest that the sharp decrease in the Zheduoshan exhumation rate since 4 Ma may be due to a transfer of activity from the Yalahe to the Selaha fault, so that the Yalahe fault may have become inactive since that time.

2.1. Slip rates review

Geologic rate estimates along the XSH fault vary between ~3.5 and 30 mm/yr, depending on whether the ~60 km geologic offset of several markers (Jinsha and Xianshui Rivers, Proterozoic and Permo-Triassic basement rocks, main Cenozoic thrusts) (e.g., Wang et al., 1998; Wang and Burchfiel, 2000; Yan and Lin, 2015) is matched with initiation ages that vary from 2 to 19 Ma (e.g., Wang et al., 1998; Roger et al., 1995; Yan and Lin, 2015; Wang et al., 2012). We however favor the ~9 Ma age of Zhang et al. (2017) hence its long-term slip-rate of ~7 mm/yr, as discussed in Bai et al. (2018).

At the late Quaternary timescale, Allen et al. (1991) inferred a rate of 15±5 mm/yr for the XSH fault, followed by quantitative studies with rates as high as ~20 mm/yr (e.g., Chen et al., 2008; Zhang et al., 2016). However, most of these rates represent maximum values because they have been obtained using the ‘lower terrace age reconstruction’ (as a riser may constantly be refreshed by the river until the lower terrace is abandoned, the age of the lower terrace corresponds to a minimum age of the offset thus to a maximum slip rate) in contrast to the ‘upper terrace age reconstruction’, which yields a maximum age for the offset thus a minimum slip rate. Ideally, one should date both the lower and upper terraces in order to bracket the slip rate (e.g., Mériaux et al.,

2012). Bai et al. (2018), using appropriate offset-age reconstructions of terrace risers from sites published by others (e.g., Chen et al., 2008; Zhang, 2013), in addition to data from their own moraine and levee sites, found rates close to 10 mm/yr along the XSH fault. At a more detailed level, what occurs NW of Kangding, where the active XSH fault splits into the three en-echelon segments is more complex. Between the Huiyansi basin and Taizhan, the active Yalahe fault is oblique to the general trend of the geologic fault (Fig. 2C), with Quaternary, left-lateral/normal, slip-rates on order of 0.6 to 2.2 mm/yr (Allen et al., 1991; Zhou et al., 2001; Chen et al., 2016). No rates yet exist farther to the SE, along the active (Allen et al., 1991; Liang et al., 2020) central part of the Yalahe fault, which is parallel to the geologic fault, nor along its SE part closer to Kangding.

Along the Selaha fault, which was inferred to be the main active segment of the SE XSH fault, Bai et al. (2018) studied three sites where the fault offsets levees and moraines: two sites NW of the Selaha pass (TG and SLH) and one site to the SE (YJG) (Fig. 2B). Using ^{10}Be dating and offset-age reconstruction, they determined late Quaternary slip-rates of 7.6*(*+2.3*/*−1.9*)* mm/yr at TG and 10.7*(*+1.3*/*−1.1*)* mm/yr at SLH, hence ~10 mm/yr assuming that the rate should be similar at these two sites located only 9 km apart. This is similar to what Allen et al. (1991) (7.2 mm/yr) or Chen et al. (2016) (6.7±3 mm/yr) had inferred between these two sites. At YJG, Bai et al. (2018) determined a much lower rate of 4.4±0.5 mm/yr, which they suggested was most likely due to the presence of the Zheduotang fault which is roughly parallel to the SE Selaha fault (Fig. 2B) hence most likely sharing its slip rate with the Selaha fault. They had thus inferred a rate of ~5 mm/yr on the Zheduotang fault, corresponding to the difference between rates at along the NW and SE Selaha fault. Other studies on the Zheduotang fault suggest slip-rates of 3 to 10 mm/yr (Zhou et al., 2001; Chen et al., 2016; Zhang et al., 2016; Yan et al., 2018).

The linear and continuous, ~50 km-long, Moxi fault located SE of Kangding, merges with the Selaha fault (Allen et al., 1991; Jiang et al., 2015a; Bai et al., 2018), similarly to the XSH fault NW of the three en-echelon segments. Almost all studies used ^{14}C dating from trenches located <9 km SE of Kangding, NW of the Xuemenkan pass (Fig. 2B), to determine the age of historical

earthquakes and suggest late Quaternary slip-rates along the Moxi fault of ~8-10 mm/yr (e.g., Zhou et al., 2001; Chen et al., 2016; Zhang et al., 2016; Yan et al., 2017). Here, we use a different approach (tectonic-geomorphology rather than paleoseismology) and technique (^{10}Be rather than ^{14}C dating) to constrain the late Quaternary slip-rate of the Moxi fault.

At the geodetic timescale, while InSAR rates along the XSH fault are on the same order (7-12 mm/yr) as the late Quaternary rates (e.g., Wang et al., 2009; Jiang et al., 2015b; Ji et al., 2020), GPS data are slightly higher, ranging from 8 to 17 mm/yr (e.g., Shen et al. 2005; Gan et al., 2007; Zhang, 2013; W. Wang et al., 2017; Y. Wang et al., 2017), even though recent estimates based on the longest GPS record (Zheng et al., 2017) suggests a constant rate of 8 to 10 mm/yr. The most recent study using elastic block (n=17) modeling of GPS data (541 stations) in SE Tibet suggests rates of 11.8±0.6 mm/yr along the Ganzi and NW Xianshuihe faults (west of its intersection with the Longriba fault), 14.5±0.9 mm/yr along the Xianshuihe fault (east of its intersection with the Longriba fault), decreasing to ~5-6 mm/yr along the Anninghe, Zemuhe and Daliangshan faults south of Moxi, and increasing again to 13.2±0.2 mm/yr along the Xiaojiang fault to the south (Wang et al., 2020) (Fig. 1). A more local GPS study across the SE XSH fault suggests rates of ~1-4 mm/yr along the Yalahe fault (Li et al., 2019; Li et al., 2020), ~6-9 mm/yr along the Selaha fault (Li et al., 2019, 2020), ~0.4-3.4 mm/yr along the Zheduotang fault (Li et al., 2020), and ~4-15 mm/yr along the Moxi fault (Li et al., 2019, Li et al., 2020).

2.2. Past earthquakes in the Kangding region

One M7 earthquake in 1700 has been reported along the Yalahe fault, with 41 km of surface ruptures (Wen et al., 2000, 2008), with ~10 km of surface rupture reported in the central part of the fault just north of Yala Mountain from remote sensing analyses and field investigation, with co-seismic horizontal offsets of gullies on order of 2.5-3.5 m (Liang et al., 2020). Along the Selaha fault, two historical earthquakes, M7 in 1725 (exact location unclear) and M6.7 in 1748, have been reported with 50 and 40 km of surface ruptures, respectively (Wen et al., 2000, 2008; Papadimitriou

et al., 2004). The recent 2014 Mw5.9 and 5.6 Kangding earthquake sequence also occurred along that fault (Jiang et al., 2015a). Along the Zheduotang fault, the 1955 Mw7.5 Kangding earthquake produced 35 km of surface ruptures (Wen et al., 2000, 2008; Zhou et al., 2001; Papadimitriou et al., 2004), recently re-evaluated by Yan et al. (2019) as only Mw7 with 43 km of surface ruptures that extend farther SE towards Moxi ('Moxi rupture' in Fig. 2B). Along the Moxi fault, two large M7.5 and M7.7 earthquakes occurred in 1327 and 1786, respectively, the latter having produced 70-90 km of surface ruptures and 2-5 m of co-seismic offsets (Zhou et al., 2001; Wen et al., 2008; Cheng et al., 2011), as well as a landslide dam across the nearby Dadu River, whose rupture ten days later following a strong aftershock, caused one of the most disastrous landslide dam failure in the world with ~100,000 casualties (e.g., Dai et al., 2005).

3. Methods

We used field investigation, as well as Google Earth and Bing high-resolution satellite imagery to map active faults and offset geomorphic features to then select the best sites along the Zheduotang (ZDT moraine) and Moxi (MX moraine) fault segments of the SE XSH fault. Offsets were precisely measured on Digital Elevation Models (DEM) obtained from Unmanned Aerial Vehicle (UAV aka drone, DJI Phantom 4 Pro) surveys at both sites and from additional surveys using a Riegel VZ1000 terrestrial LiDAR (Light Detection and Ranging) (angular resolution of 0.02° for raw data, set to 0.5 m between two data points after process) at the MX site.

We collected nine samples from the lateral moraine crest at the ZDT site, 11 samples from that at the MX site, and another five samples from an inner moraine crest at the MX site, from the top few centimeters of large, stable, well-embedded granite boulders (1-4 m in diameter, Figs. S1-S3) using chisel and hammer. Collecting such a large number of samples on individual moraine crests has been our team's moto, which greatly increases the likelihood to date the actual age of the moraine (Chevalier et al., 2011, 2019). We use cosmogenic ^{10}Be surface-exposure dating (e.g., Lal, 1991; Gosse and Phillips, 2001) to constrain the moraine abandonment ages (i.e., the onset of

deglaciation) following mineral separation and quartz cleaning procedure modified from Kohl and Nishiizumi (1992). Model ages were calculated using CRONUS v3 (Balco et al., 2008) with the Lm (Lal [1991]/Stone [2000]) and LSDn (Lifton et al., 2014) production rate models (Table 1) and we refer to the Lm ages (Lal [1991]/Stone [2000]; time-dependent) in the text. We then combine the moraine abandonment age with their offsets to reconstruct the space-time evolution of the faults and determine their late Quaternary slip-rates (median rates are calculated using the Gaussian uncertainty model of Zechar and Frankel, 2009).

Ideally, one wants to sample boulders that have been exposed on moraine crests since deglaciation, with no rolling, shielding or surface erosion since deposition (which tend to skew the ages toward values younger than the actual age), and no exposure prior to deposition (which tends to skew ages toward older values). These old ages however, are thought to be occasional (e.g., Hallet and Pukonen, 1994; Putkonen and Swanson, 2003; Heyman et al., 2011), especially since rocks have been pulled off from the glacial valley, crushed, and eroded before settling on a moraine's crest. Such outliers may be singled out and discarded using statistical tests such as Chauvenet (Bevington and Robinson, 2002) or Peirce criteria. Four (three young and one old) outliers were found on MX main crest, one young one on MX inner crest and two old ones on ZDT crest. After rejecting them, we assign a class (A for well-, B for moderately- and C for poorly-clustered ages) to each moraine, using reduced Chi-square analyses (see Chevalier and Replumaz, 2019; following Heyman, 2014). While the average age is taken to represent the most likely abandonment age of Class A moraines, the oldest age is instead taken for Classes B and C moraines (Heyman, 2014) because even though moraines are relatively stable landforms over the long term, crests are slowly adjusting following their abandonment, with boulders being gradually exhumed to the surface (hence their younger ages), thus representing multiple stages of exhumation as the surface lowers due to erosion of the matrix (e.g., Chevalier and Replumaz, 2019). Therefore, and because we assume zero erosion and did not correct for snow and vegetation cover, the apparent ages we calculate are minimum ages. Eventually, we assign a Marine oxygen Isotope Stage (MIS)

(e.g., Lisiecki and Raymo, 2005) to each moraine which indicates the climatic period during which the moraine was deposited and abandoned.

4. Sites description and results

We describe the faults and study sites from NW to SE along the SE XSH fault. First, we introduce our preliminary results attesting of the central Yalahe fault activity, just north of Yala Mountain, then describe the newly discovered 'Mugecuo South' fault zone trace located on the NE flank of the Zheduoshan Range between the Selaha and Zheduotang faults. We then present the two study sites, ZDT moraine along the Zheduotang fault and MX moraine along the Moxi fault.

4.1. Yalahe fault

The Yalahe fault constitutes the NE branch of the right-stepping en-echelon faults of the active SE XSH fault (Fig. 2B). It runs from the eastern Huiyuansi basin where it strikes ~N110°E, cuts across the slopes of the Taizhan valley and merges with the ~N140°E-striking Yalahe geologic fault along the northern side of Yala Mountain (peak at 5820 m), where it more or less follows the Yalahe valley for 18 km until it reaches Kangding city (Fig. 2B,C). The Yalahe geologic fault extends 130 km NW of Taizhan before merging with the XSH fault. Near Taizhan, the granitoids are affected by a ~1.3 km-wide zone of ductile and brittle deformation linked to the left-lateral Yalahe fault (Chen et al., 1985). The northern boundary of the Gongga-Zheduoshan batholith shows an apparent minimum offset of 15 km but the offset of the southern boundary may be as large as 50 km (Bai et al., 2018) (AA’ and BB’ in Fig. 2C).

The active NW part of the fault bounds the SE Huiyuansi basin, which was created thanks to the significant oblique (left-lateral/normal) component of motion along the fault, in agreement with its oblique strike direction compared to that of the main XSH fault (e.g., Allen et al. 1991) (Fig. 2B). From aerial photograph analyses (Allen et al., 1991) and field investigation (Liang et al., 2020), it is clear that the central part of the fault between ~Taizhan and Yala Mountain is also active.

The fault can be followed for ~7 km on satellite images, and during our own field investigation, we found a ~1 m-high fault scarp for ~2.4 km (Fig. 3), i.e., a total of at least ~10 km, as recently reported by Liang et al. (2020), who also found several co-seismic (2.5-3.5 m) as well as one cumulative (~15 m) horizontal offsets along that section. Just SE of Yala Mountain however, in the large U-shaped Yalahe valley (Fig. 3B), the fault trace cannot easily be followed on satellite images, either because this section may be inactive at present with activity having been transferred to the Selaha fault (e.g., Zhang et al., 2017; Bai et al., 2018), or because of the dense vegetation making remote sensing analyses difficult. Extra field work is clearly necessary to constrain the behavior of the Yalahe fault along that SE section. While Allen et al. (1991) found no evidence of the Yalahe fault farther SE closer to Kangding, most likely due to the numerous villages in that valley hindering precise aerial mapping due to human modifications, Liang et al. (2020) reported it from cross-sections at a few locations (Fig. 2B).

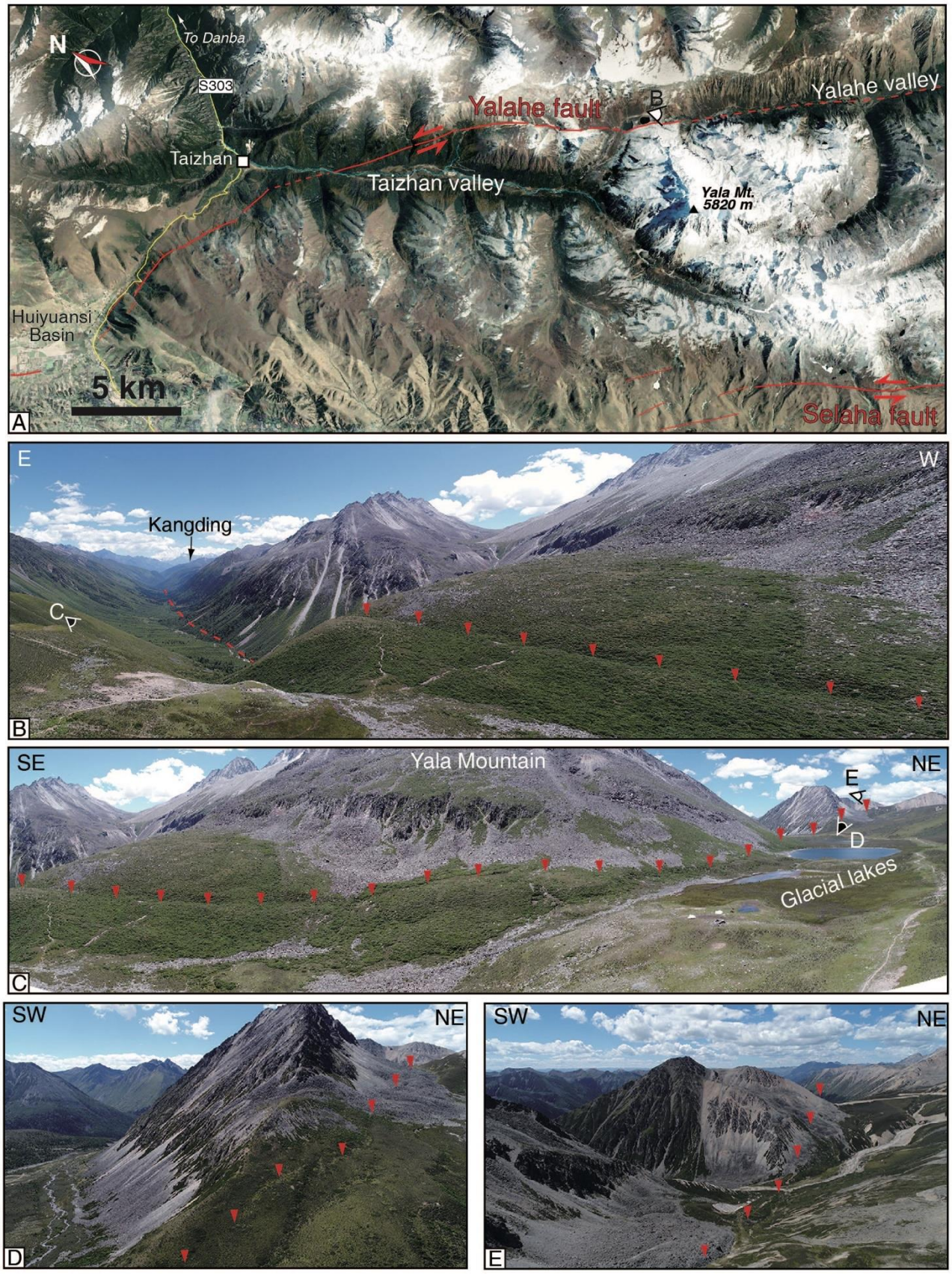

Figure 3: *The Yalahe fault. (A) Google Earth image of the Yalahe fault between the Huiyuansi Basin and Yalahe valley. Legend as in Figure 1. (B) View looking south along the Yalahe fault, with clear, linear, fault scarp. Farther south, the fault trace becomes hard to follow. (C-E) Fault trace along the glacial lakes and farther to the NW.*

4.2. Selaha fault and Mugecuo releasing bend

While the Selaha fault is thought to be the main active branch of the SE XSH fault (Bai et al., 2018), its trace between the Selaha pass and Mugecuo Lake is not as clear as that farther NW and SE (Fig. 2B). To the NW, morphological evidence for active faulting abound along a linear N150° trend along which the TG and SLH sites of Bai et al. (2018) are located (Fig. 2B), following the geological fault that separates the Gongga-Zheduoshan batholith from Triassic sediments (Chen et al., 1985) (Fig. 2C). The fault left-laterally offsets the batholith edges by ~15 km (Roger et al., 1995; Bai et al., 2018) (CC' in Fig. 2C). To the SE, the fault is continuous and linear again where Bai et al. (2018)'s YJG site is located (Fig. 4A,E), trending N154° and corresponding to the limit between two granitoids of the batholith (Fig. 2C). Between these two linear fault splays, Mugecuo Lake (Fig. 4A) now fills what is considered as a 5 km-long releasing bend (Allen et al., 1991; Bai et al., 2018), but individual fault traces were not clearly documented until now. The steep topographic slope marking the north bank of Mugecuo Lake corresponds to the morphological expression of a more recent normal fault trending N120° and is cut by several topographic scarps that we interpret as secondary faults (Fig. 4A). South of the lake, the NE slope of the Zheduoshan Range is less steep but our UAV surveys (Fig. 4B,C) followed by Pan et al. (2020)'s field survey (Fig. 4D), revealed for the first time, countless topographic scarps up to ~10 m-high that can be followed for ~22 km (Fig. 4A). We interpret these scarps as the morphological expression of active normal faults trending N110° to N140° and termed the 'Mugecuo South fault zone' (Pan et al., 2020). These observations confirm that the Mugecuo Lake area is a releasing bend between the two linear splays of the Selaha fault, located within a large-scale push-up (e.g., Gaudemer et al., 1995).

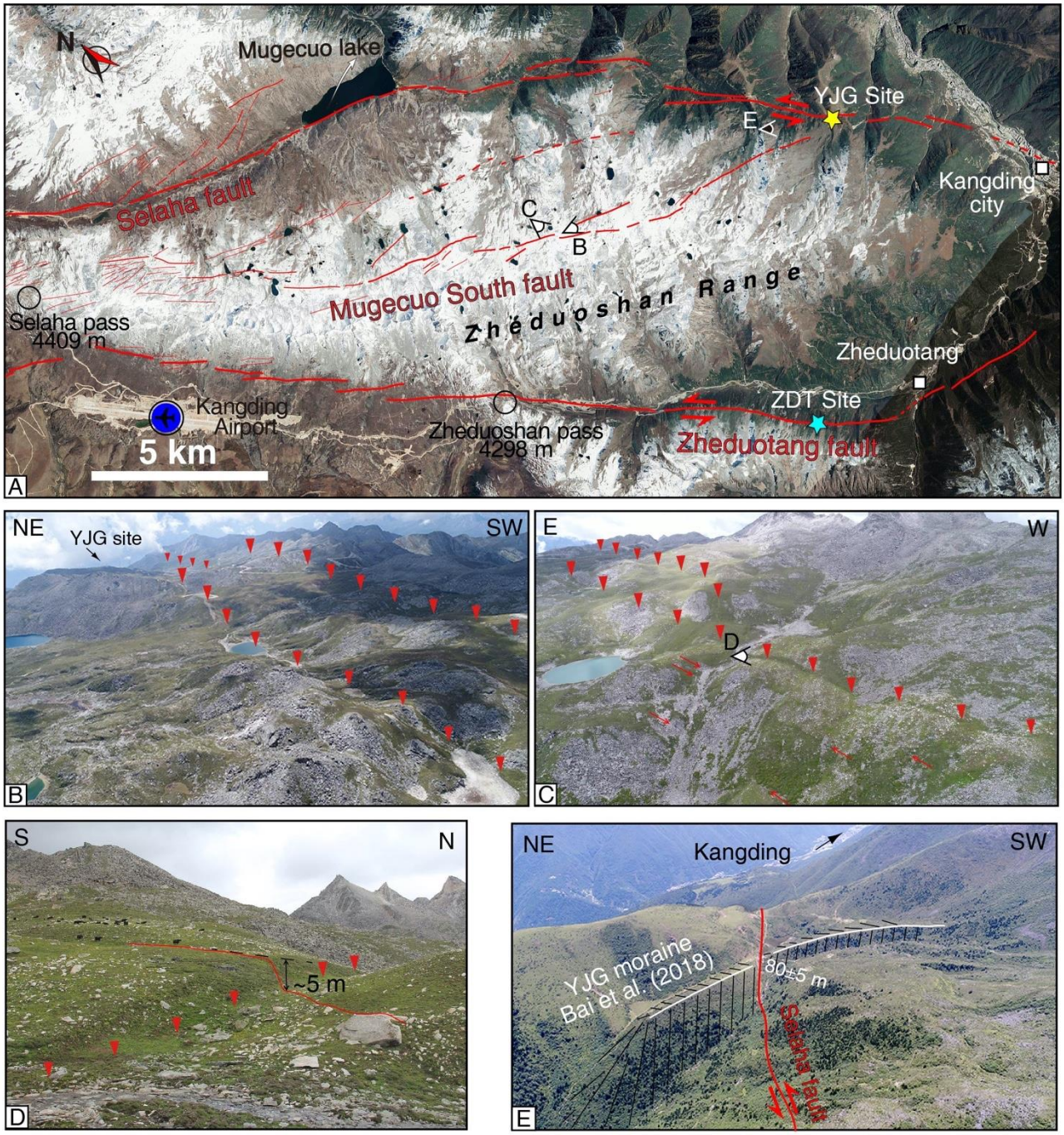

339

340 ***Figure 4:*** *Mugecuo South fault zone and releasing bend. (A) Google Earth image of the Selaha,*
341 *Zheduotang and Mugecuo South fault zone strands between the Selaha pass and Kangding. Legend*
342 *as in Figures 1 and 2. (B,C) UAV photos of faults from the Mugecuo South fault zone highlighted by*
343 *red triangles and arrows. (D) Field photo of a ~5 m fault scarp along the Mugecuo South fault*
344 *zone. (E) UAV photo of the YJG site from Bai et al. (2018), taken from the Mugecuo South fault*
345 *zone.*

346

347 **4.3. The Zheduotang fault and ZDT site**

348 The ~N145°-striking Zheduotang fault left-laterally offsets the western boundary of the

Gongga-Zheduoshan batolith by ~10 km (Bai et al., 2018) (DD' in Fig. 2C). Its morphological trace is clear for ~27 km: ~13 km on the SW slopes of the Zheduoshan Range, from Kangding airport (third highest airport in the world, 4280 m) to the Zheduoshan pass, before becoming hard to follow in the valley due to the Kangding-Lhasa highway (and its numerous emergency side accesses), until it reaches the mountain slopes on the other side of the valley (Fig. 4A). There, the Zheduotang fault sharply cuts about half-way for ~7 km, the NE-facing, steep (~34°), slopes on which numerous rockslides are present (Fig. 5A,D). It is along that section that the fault best displays left-lateral offsets of moraines (Fig. 5A-C). Farther to the SE, the fault reaches the valley again at Zheduotang village and cuts the mountain slopes for another ~2 km before it becomes hard to follow (Fig. 5A). The fault has a slight normal component of motion with SW (uphill)-facing scarps, resulting in numerous sag ponds along the fault, particularly impressive along the section between the highway and Zheduotang village where the scarps can reach 8-10 m-high (Fig. 5D,E).

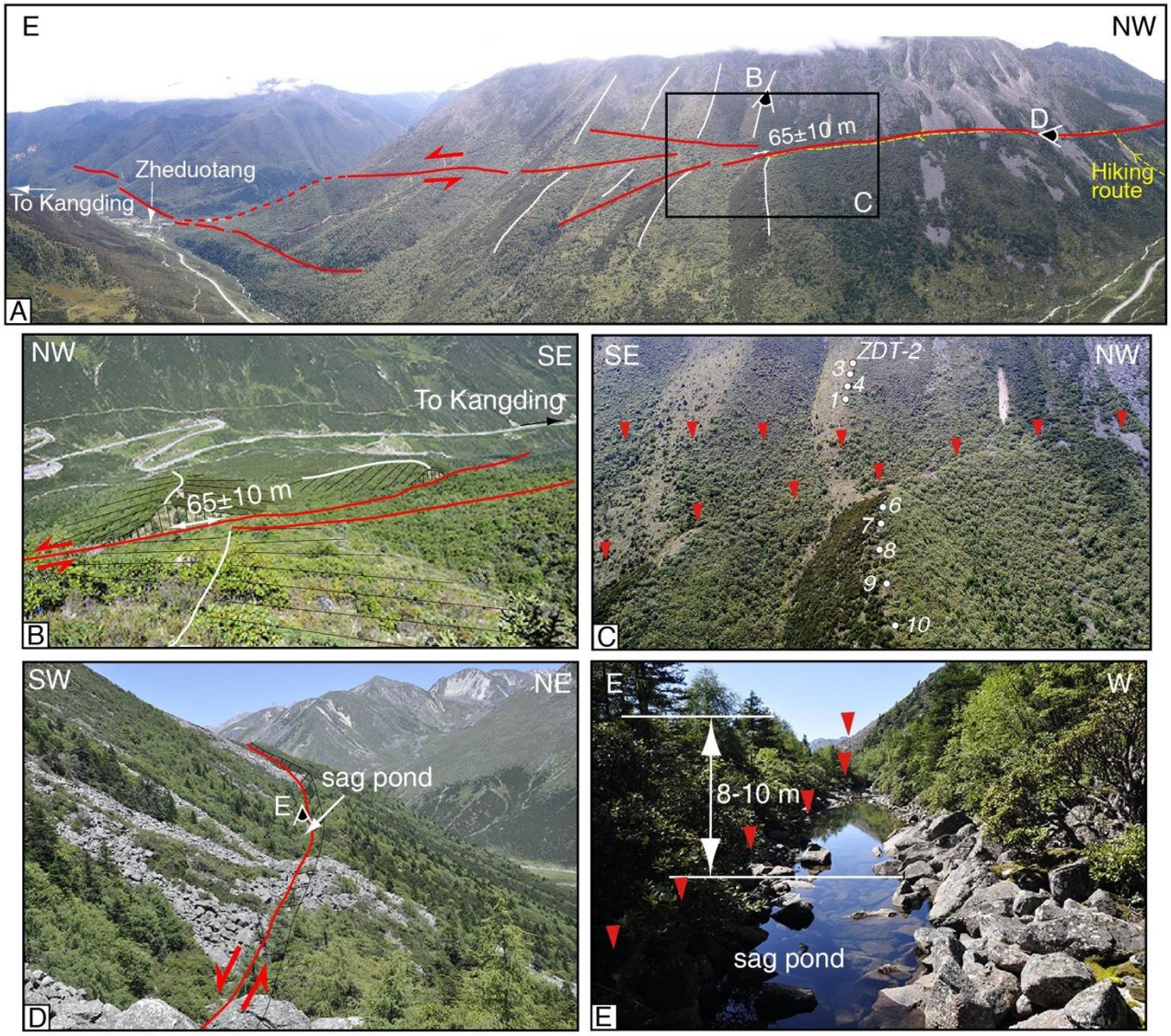

Figure 5: *Zheduotang fault and ZDT site. (A) Panoramic UAV photo of the SE segment of the Zheduotang fault with white lines highlighting the offset moraine crests. (B) Photo looking downstream at the ZDT lower crests and the 65 m left-lateral offset. (C) UAV photo of the ZDT moraine with white circles and numbers representing collected samples. (D) Photo of the uphill-facing fault scarp where numerous sag ponds are present. (E) Photo of an uphill-facing, 8-10 m-high, fault scarp.*

The remote Zheduotang (ZDT) moraines are located along that section, ~ 10 km due west of the city of Kangding, at ~3860 m of elevation (Figs. 2B and 5). Their sub-rounded crests are ~1 km-long and are covered with medium-sized granite boulders (~1 m of diameter) (Fig. S1). While the upper crest is only covered with small bushes and occasional trees, the lower crest is covered with denser vegetation, especially on its outer slope (Fig. 5C). The Zheduotang fault cuts and left-

laterally offsets the ZDT moraines by 65±10 m (Figs. 5 and 6). The steep slopes, extremely dense vegetation at lower elevations, numerous rockslides with extremely large, angular, boulders, and the large stream at the base of the mountain slopes (difficult to cross), all made this site extremely challenging to reach. We eventually were able to collect a total of nine samples from the NW crest: five upstream from the fault (ZDT-1-4) and five downstream (ZDT-6-10) (Fig. 5C). Ages range from 12.7±1.0 ka to 30.0±2.4 ka (Fig. 7 and Table 1). Applying statistical tests allows to discard the two oldest samples, with the remaining seven samples being well-clustered (moraine is Class A), ranging from 12.7±1.0 to 15.9±1.2 ka. Therefore, the average age, 14.3±1.1 ka, is taken to represent the moraine's abandonment age. Combining offset and age yields a left-lateral slip-rate of 4.5(+0.9/-0.8) mm/yr.

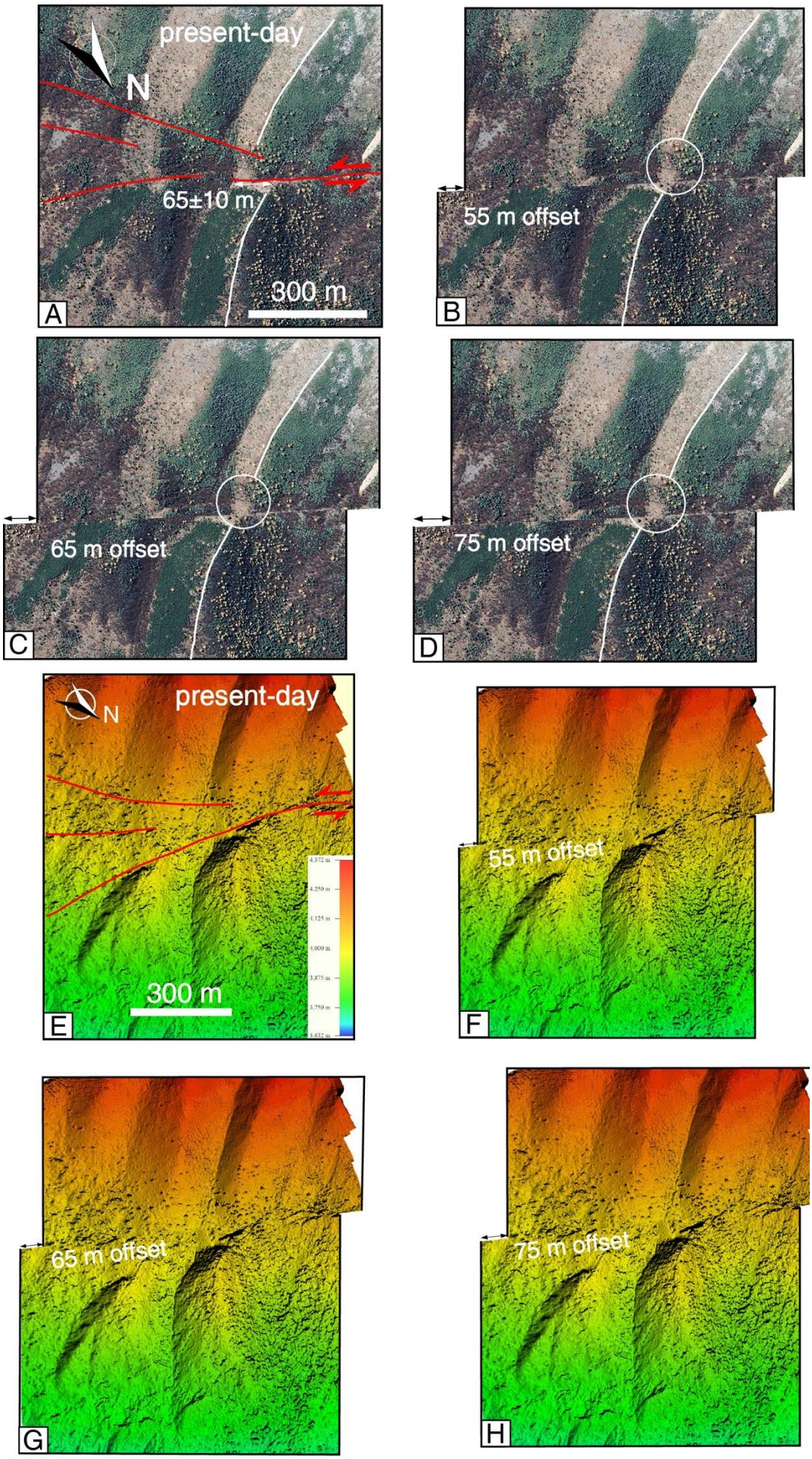
present-day
N
65±10 m
300 m
A
55 m offset
B
65 m offset
C
75 m offset
D
N
present-day
300 m
E
55 m offset
F
65 m offset
G
75 m offset
H

384

Figure 6: *Offset at the ZDT site. (A-D) Google Earth images and (E-H) DEM obtained from our UAV survey of the ZDT moraine and their offset reconstructions.*

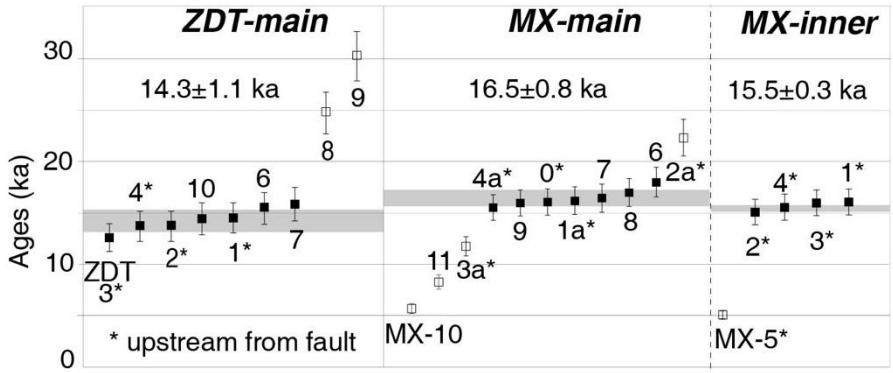

Figure 7: *^{10}Be cosmogenic surface-exposure ages of the ZDT and MX moraines, calculated using CRONUS v3 (Balco et al., 2008), with 'Lm' production rate model (Lal (1991)/Stone (2000) time-dependent model). Outliers (in open symbols) were determined using Chauvenet and Peirce criteria (see text for details).*

Table 1: *Analytical results of ^{10}Be geochronology and surface-exposure ages along the Zheduotang and Moxi faults.*

Sample name	Lat (°N)	Long (°E)	Elev.	shielding	10Be(at/g)	Lm ages (yrs)	Int. Uncert.	LSDn ages (yrs)	Int. Uncert.
ZDT site									
upstream									
ZDT-1	30.007218	101.853394	3938	0.97	582604±9527	**14523±1132**	241	14815±922	246
ZDT-2	30.007075	101.852399	4024	0.97	569669±11427	**13748±1083**	280	13920±881	283
ZDT-3	30.007142	101.85266	3998	0.97	506680±9258	**12655±990**	234	12908±808	239
ZDT-4	30.007173	101.853023	3954	0.97	544843±12160	**13643±1083**	309	13863±888	314
downstream									
ZDT-6	30.008677	101.855455	3818	0.97	588013±11776	**15418±1217**	314	15771±1000	321
ZDT-7	30.00863	101.855689	3813	0.97	604810±11605	**15863±1249**	310	16259±1027	318
ZDT-8#	30.008681	101.856037	3831	0.97	1018291±17250	**24910±1968**	434	25226±1591	439
ZDT-9#	30.009041	101.856574	3796	0.97	1222029±15333	**30046±2360**	389	30494±1901	395
ZDT-10	30.00918	101.856736	3779	0.97	534327±9037	**14453±1129**	248	14817±924	255
Moxi site									
upstream									
MX-0	29.88182	102.009519	3877	0.99	644968±14438	**16099±1282**	373	16434±1056	382
MX-1a	29.881898	102.009739	3879	0.99	651371±19511	**16231±1334**	504	16556±1115	516
MX-2a#	29.881799	102.00999	3879	0.99	941220±19057	**22354±1779**	472	22654±1448	479
MX-3a#	29.881875	102.01018	3868	0.99	448416±10022	**11810±936**	273	12148±777	281
MX-4a	29.881813	102.010269	3870	0.99	620232±14033	**15559±1240**	365	15905±1022	374
downstream									
MX-6	29.883161	102.011295	3865	0.99	726534±15952	**18029±1437**	411	18470±1186	421
MX-7	29.883558	102.010804	3887	0.99	666039±21318	**16481±1368**	548	16866±1153	560
MX-8	29.880397	102.011228	3881	0.99	686869±13617	**17022±1345**	350	17392±1103	358
MX-9	29.882661	102.012665	3862	0.99	636352±12761	**16002±1264**	333	16361±1038	340
MX-10#	29.882107	102.0135603	3838	0.99	196027±6791	**5748±478**	204	6031±415	214
MX-11#	29.879169	102.016253	3777	0.99	290547±8810	**8329±680**	260	8714±584	273
inner moraine									
MX-1	29.881255	102.007344	3908	0.99	643607±13986	**15815±1256**	357	16179±1035	364
MX-2	29.881301	102.00653	3929	0.99	618110±11154	**15107±1185**	282	15372±964	288
MX-3	29.881281	102.008223	3900	0.99	637961±11949	**15744±1238**	306	16107±1015	312
MX-4	29.881281	102.009237	3876	0.99	618939±19361	**15486±1280**	502	15821±1075	514
MX-5#	29.880635	102.009737	3862	0.99	171435±6838	**5113±437**	209	5325±381	217

Samples were processed at the Institute of Crustal Dynamics, China Earthquake Administration, Beijing, and the 10Be/9Be ratios were measured at GNS Science in New Zealand.

Ages are calculated with the CRONUS v3 calculator (Balco et al., 2008). Sample names with # represent outliers that were statistically rejected (see text). All samples are granite (density 2.7 g/cm3); Shielding factor is 0.99 and 0.97 for

Moxi and ZDT sites, respectively. Thickness is 5cm.
No erosion rate was applied. Standard used at GNS is '01-5-4', with 10Be/9Be = 2.851e-12.
Lm=Lal (1991)/Stone (2000) time-dependent production rate model; LSDn=Lifton et al. (2014) production rate model.

4.4. The Moxi fault and MX site

The NNW-striking Moxi fault runs from Kangding to Moxi cities, lying between the Proterozic Kangding igneous complex and slivers of Paleozoic rocks (Lu et al., 1975; Liu et al. 1977). The fault shows evidence of recent faulting along its northern section where it cuts through the western slopes of the Lamo-She Range, crosses the Xuemenkan pass (~4000 m) then cuts through the eastern slopes of the Daxue Range (where Gongga Shan lies) (Fig. 8A). It is along that section that the fault is the clearest, with numerous offsets of moraines, gullies, and alluvial fans, forming sag ponds at places thanks to its slight normal component of motion, with NE-facing scarps to the north and SW-facing scarps to the south. While the main Moxi fault lies quite low on the mountain slopes, numerous other fault strands are present higher on the slopes near the Xuemenkan pass (Fig. 8A) (Yan et al., 2019), with W to SW-facing scarps damming sag ponds. Seven km SE of the pass, the fault trace becomes harder to follow because it reaches the Moxi valley filled where large streams (coming directly from Gongga Shan), huge fluvio-glacial terraces and rockslide deposits abound.

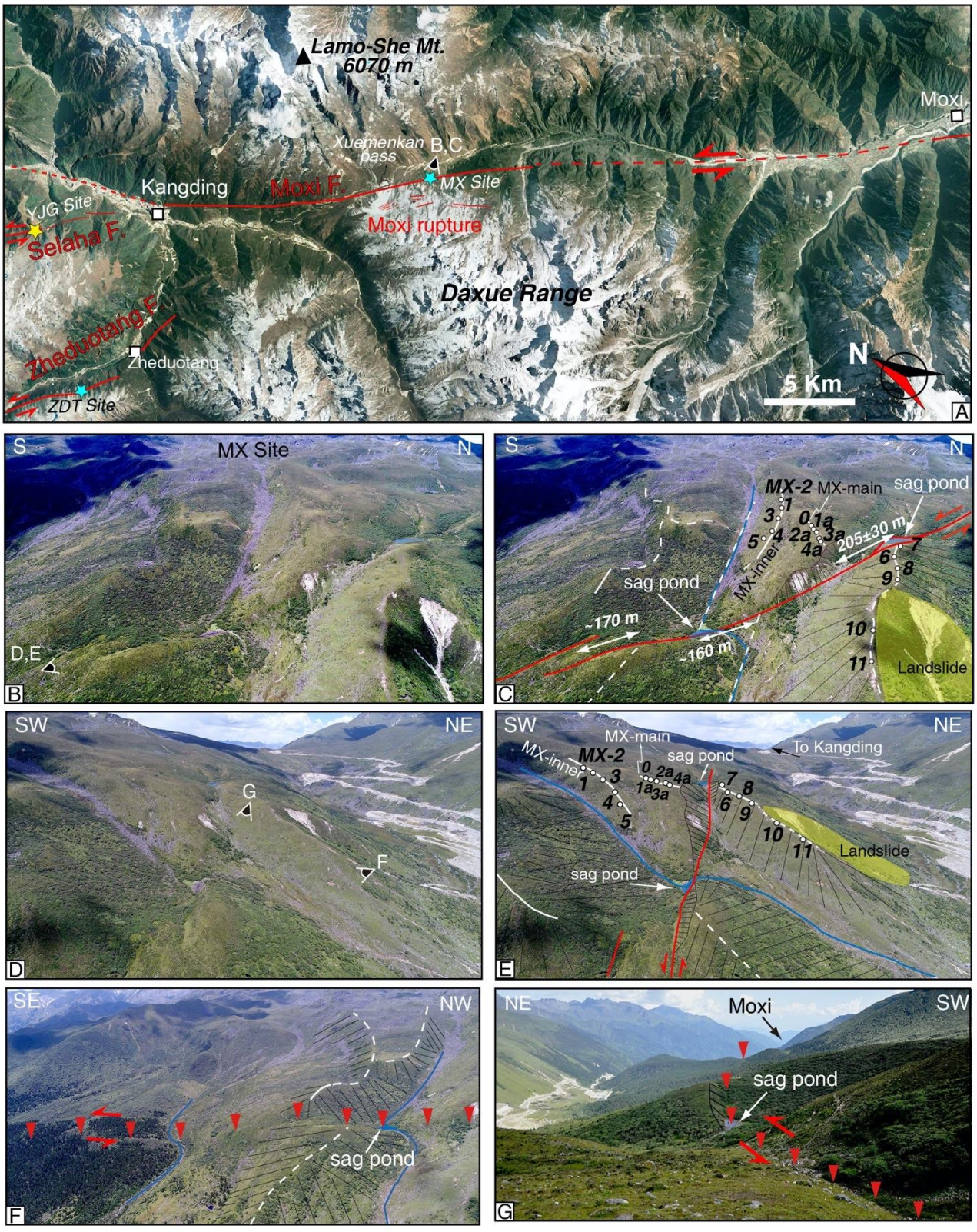

418

419 ***Figure 8:*** *Moxi fault and MX site. (A) Google Earth image of the Moxi, SE Zheduotang and Selaha*
420 *faults. Legend as in Figures 1 and 2. (B-E) UAV photos of the MX moraines and their*
421 *interpretation. (F) Fault trace and offset of southern moraine. (G) Fault trace and sag pond about 2*
422 *km south of the MX site.*

423

The ~1.5 km-long Moxi (MX) moraines are located along the segment just SE of the Xuemenkan pass, ~ 15 km SE of Kangding, at ~3850 m of elevation (Fig. 8). While the main MX moraine crosses the Moxi fault, the inner moraine does not. The moraine crests are sub-rounded and covered with small bushes, and with medium (on the main moraine) to large (on the inner moraine) granite boulders (Figs. S2 and S3). A landslide removed part of the main moraine downstream from the fault (Fig. 8). Thanks to the left-lateral motion on the Moxi fault, two sag ponds at the base of the resulting SW-facing scarps formed, larger at the base of the northern crest (north of the stream, Fig. 8). The main northern and southern (south of the stream) MX moraine crests are left-laterally offset by 205±30 and ~170 m, respectively (Fig. 9). A smaller offset for the southern crest is excepted due to the sense of motion of the Moxi fault, with the stream in between, whose offset is ~160 m at present, constantly refreshing the lateral slopes.

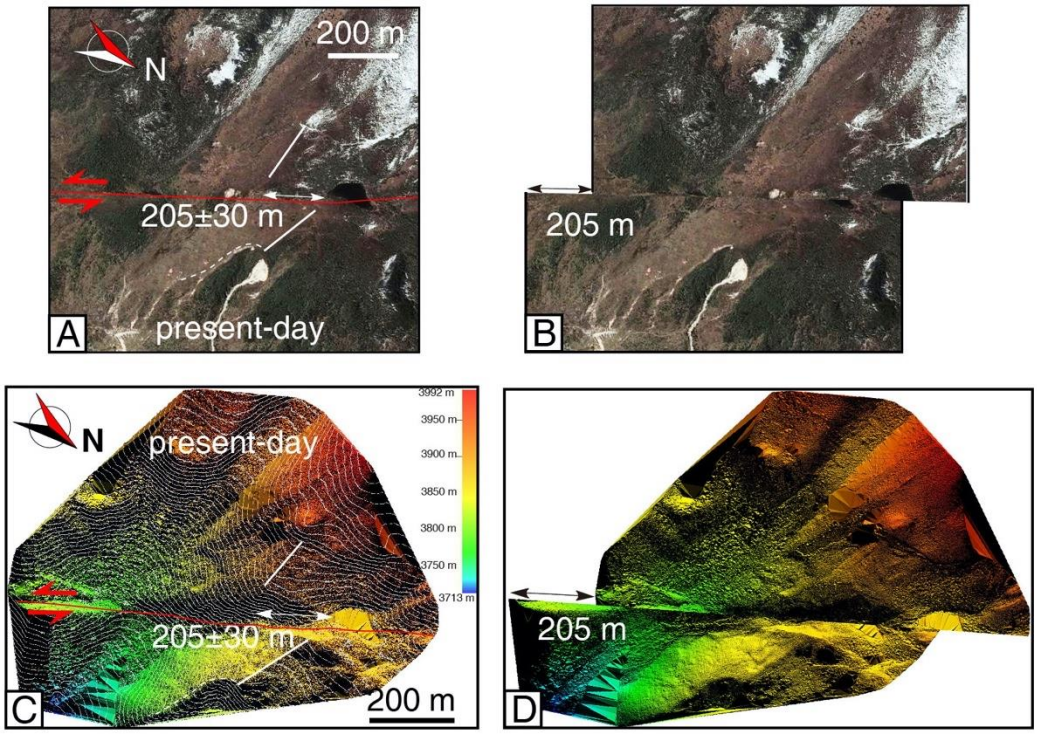

Figure 9: *MX site offsets. (A,B) Google Earth and (C,D) LiDAR DEM of the MX moraine and their offset reconstruction.*

We collected 16 samples at the MX site along the northern crests, five on the inner moraine crest (MX-1-5), five upstream from the fault on the main MX crest (MX-0, MX-1a-4a) and six

downstream (MX-6-11) (Fig. 8B,D). Ages on the inner crest range from 5.1±0.4 to 15.8±1.3 ka and those on the main crest range from 5.7±0.5 to 22.3±1.8 ka (Fig. 7 and Table 1). Applying statistical tests allows to discard the youngest sample on the inner crest as well as the three youngest and the oldest samples on the main crest. It is interesting to note that all the young outliers are located the farthest downstream, most likely reflecting material removal due to the landslide, which has reshaped the crest to its present-day geometry. The original crest may thus only be preserved close to the fault, where samples MX-6 to 9 are located. The four and seven remaining samples on the inner and main crest cluster very well and the moraines are Class A. Therefore, their average age is taken to best represent their abandonment age: 15.5±0.3 ka for the inner moraine and 16.5±0.8 ka for the main moraine. Combining the offset and the age of the main, northern moraine yields a left-lateral slip-rate of 12.5(+2.3/-2.1) mm/yr.

5. Discussion

5.1. Slip distribution in the SE Xianshuihe fault and southeastward rate increase

In the SE XSH fault near the Huiyuansi Basin, the geometry of the XSH fault changes dramatically from a single, linear and continuous trace to the three en-echelon faults discussed here. Bai et al. (2018), using the same technique as in this paper, determined rates of 9.6-9.9 (TG and SLH sites) and 4.4±0.5 (YJG site) mm/yr along the NW and SE parts of the Selaha fault, respectively. This led them to infer that the Zheduotang fault, which is parallel to the SE Selaha fault, may slip at ~5 mm/yr in order to match the total slip rate in the SE with that along the NW Selaha fault. Our study at the ZDT site allows us to determine a late Quaternary (~15 ka) rate of 4.5(+0.9/-0.8) mm/yr, in agreement with Bai et al. (2018)'s inference, suggesting that recent motion on the NW Selaha fault is partitioned between the SE Selaha fault and the parallel Zheduotang fault. However, at a more detailed level, the slip rate along the XSH fault and NW Selaha fault (~10 mm/yr) appears ~1 mm/yr faster than that farther to the SE, across both the SE Selaha and Zheduotang faults (~9 mm/yr). This difference may be absorbed by the Yalahe (if active closer to

Kangding) and Mugecuo South fault zone and releasing bend, where numerous, mostly normal with minor left-lateral component, fault strands are present. The total rate is similar to the present-day rate (11.7±1.5 mm/yr across the Yalahe, Selaha and Zheduotang faults, Table 2) suggested by Li et al. (2020) from a 2D elastic dislocation model based on GPS velocities (2004-2017), and assuming a locking depth of 15 km. SE of Kangding, where the fault becomes linear and continuous again as the Moxi fault, we determined a rate of 12.5(+2.3/-2.1) mm/yr at the MX site. This rate should be considered as a minimum because several minor fault strands are located upstream (west) from our site, and most likely also absorb part of the deformation.

Table 2: *Slip rates summary along the SE Xianshuihe fault.*

Segment	Slip-rate (mm/yr)	Reference	Method
Yalahe fault	2.3±1.5	Li et al. (2020)	GPS + earthquake relocation
	2±0.2	Zhou et al. (2001)	thermoluminescence and 14C ages
	0.6-1.5	Chen et al. (2016)	one thermoluminescence age
Selaha fault	7.5±1.6	Li et al. (2020)	GPS
	6.14	Li et al. (2019)	Gravity and GPS data
	5.5±0.6	Zhou et al. (2001)	thermoluminescence and 14C ages
	9.75±0.15	Bai et al. (2018)	10Be (TG and SLH sites, NW Selaha fault)
	4.4±0.5	Bai et al. (2018)	10Be (YJG site, SE Selaha fault)
Zheduotang fault	1.9±1.5	Li et al. (2020)	GPS
	8.5±2	Chen et al. (2016)	one 14C, one OSL age
	5±1	Zhang et al. (2016)	14C
	3.5±0.3	Zhou et al. (2001)	14C
	3.4±0.4	Yan et al. (2018)	14C
	4.5(+0.9/-0.8)	**This study**	10Be (ZDT site)
Moxi fault	7.2– 14.7	Jiang et al. (2015b)	3D visco-elastic model with InSAR and GPS data
	4.41	Li et al. (2019)	Gravity and GPS data
	9.9±0.6	Zhou et al. (2001)	14C
	9.3±1	Chen et al. (2016)	14C
	8.47±0.92	Zhang et al. (2016)	one thermoluminescence age
	~10	Yan et al. (2017)	14C
	12.5(+2.3/-2.1)	**This study**	10Be (MX site)

From NW to SE, the late Quaternary slip rate along the Xianshuihe fault system increases from ~6-8 mm/yr along the Ganzi fault (Chevalier et al., 2017) to ~10 mm/yr along the XSH fault (e.g., Bai et al., 2018, this study), to ~12.5 mm/yr along the Moxi fault. It has been suggested that part of this increase is linked to interaction with the Longriba fault (Bai et al., 2018; Wang et al., 2020). Indeed, the GPS vectors with respect to Eurasia (e.g., W. Wang et al., 2017, 2020; Wang and Shen, 2020; Xu et al., 2020) located north of the Longriba fault show that the Bayan Har block

moves faster towards the east, than the Longmenshan block located SE of that fault (Fig. 1). Similarly, the Longmenshan block itself moves faster to the east than the Sichuan Basin located farther SE of the Longmenshan (LMS in Fig. 1). By contrast, motion of the Chuandian block SE of the XSH fault is more homogenous, thus resulting in a faster rate absorbed by the Moxi fault compared to the XSH fault, itself faster than the Ganzi fault (Fig. 10). South of Moxi, it is debated whether the rate increases, decreases, or remain rather constant along the Annighe-Zemuhe-Xiaojiang faults of the Xianshuihe fault system (e.g., He et al., 2009; Zheng et al., 2017; Wang et al., 2020).

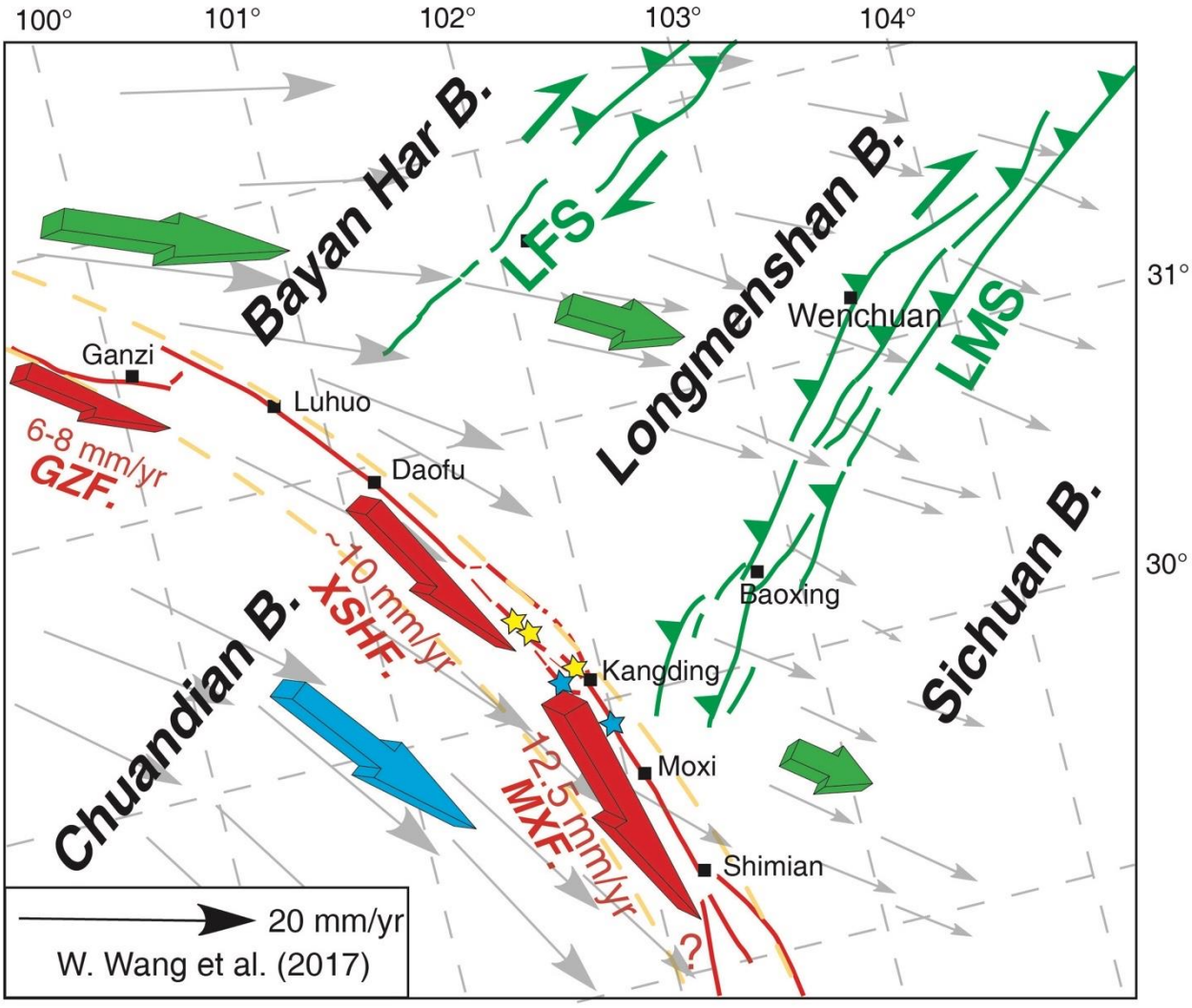

Figure 10: *Conceptual 2D model of the Xianshuihe fault following the India–Asia collision (modified from Bai et al., 2018). Red arrows show the southeastward slip rate increase, with rates from Chevalier et al. (2017) along the Ganzi fault (GZF), Bai et al. (2018) along the Xianshuihe/Selaha fault (XSHF), and this study along the Zheduotang and Moxi (MX) faults.*

LFS=Longriba fault system, LMS=Longmenshan. Orange dashed line shows how well a small circle whose pole of rotation is located in the eastern Himalayan syntaxis fits the trace of the Xianshuihe fault system. Grey arrows show GPS vectors relative to stable Eurasia (W. Wang et al., 2017). Green and blue arrows show the block movement on each side of the Xianshuihe fault system with their appropriate lengths according to the GPS velocities. Red arrows show slip rates on each segment of the Xianshuihe fault system, with their respective values indicated. Yellow and blue stars show location of sites from Bai et al. (2018) and this study, respectively.

5.2. Seismic hazard in the Kangding region

Satellite images analysis and field investigation confirmed that at least the NW and central segments of the Yalahe fault are active with recent, as well as cumulative, offsets, while the potential activity along the SE part needs to be assessed. Taking a ~1 mm/yr rate (as suggested for the NW part), a slip deficit of only ~30 cm would have accumulated since the last large earthquake in 1700 (M7). This would correspond to a Mw6.5 to 7.2 earthquake hazard at present if the entire ~75 km of the fault would rupture (Wells and Coppersmith, 1994), or to a Mw6.5 to 6.9 earthquake hazard considering a similar rupture length (41 km) as that of the 1700 earthquake (Wen et al., 2000).

Our recent field investigation along the Mugecuo South fault zone revealed numerous fault strands as well as cumulative fault scarps up to ~10 m-high (Pan et al., 2020). Although its geometry is different from that of the more linear and continuous traces of the Yalahe, Selaha, and Zheduotang faults, the numerous faults at the surface may connect at depth, so that large earthquakes may still occur, especially because of the regional Coulomb stress increase following the 2008 Wenchuan earthquake (e.g., Parsons et al., 2008), as well as because the energy accumulated in the region since the 1955 Mw7.5 Kangding earthquake was only partly released during the 2014 Mw5.9 and 5.6 Kangding earthquake sequence (e.g., Jiang et al., 2015a; Xie et al., 2017). In any case, geophysical studies all indicate a high seismic hazard in the Kangding region (e.g., Jiang et al., 2015a, NSPRC 2016; Wang and Shen, 2020), with a possible M6.5-6.8 earthquake risk at present determined from geologic studies (Bai et al., 2018), which would be especially

catastrophic due to the steep slopes surrounding the city, resulting in landslides and mud flows, as observed after the Wenchuan earthquake (e.g., Gorum et al., 2011). Lastly, taking our ~12.5 mm/yr rate would correspond to a slip deficit of ~3 m since the last large (M7.75) earthquake along the Moxi fault in 1786, which produced 70-90 km of surface ruptures (e.g., Zhou et al., 2001). This would correspond to a potential earthquake as high as Mw7.3 at present, which would devastate Moxi town, which, despite currently being less populated than Kangding city, continuously expands to cater to increasing tourism, thanks to its location at the base of Gongga Shan.

6. Conclusion

By studying four locations along the three en-echelon faults of the SE Xianshuihe fault, the Yalahe, Selaha and Zheduotang faults, as well as along the Moxi fault to the SE, we:

(1) Determined that the late Quaternary slip rate along the Zheduotang fault is 4.5(+0.9/-0.8) mm/yr, hence confirming Bai et al. (2018) inference.

(2) Determined that the minimum rate across the SE Selaha and parallel Zheduotang faults is ~8.9±1.4 mm/yr, to which one may add that across the Mugecuo South fault zone, where a series of active faults with mostly normal (and left-lateral) component of motion absorb part of the deformation.

(3) Suggest from field investigation, that the central part of the Yalahe fault is active, with clear fault scarps that can be followed for ~10 km. While slip rates are still lacking, it may also slightly contribute to the total slip rate of the SE Xianshuihe fault.

(4) Determined that SE of Kangding, the late Quaternary slip rate along the Moxi fault is 12.5(+2.3/-2.1) mm/yr, which is larger than the ~10 mm/yr along the Xianshuihe fault, and larger than the ~6-8 mm/yr rate along the Ganzi fault. This southeastward rate increase until at least Moxi is in agreement with the observed eastward rate decrease observed from GPS vectors located north of the Xianshuihe fault system, from the Bayan Har block to the Longmenshan block, as well as from the Longmenshan block to the Sichuan Basin.

(5) Suggest that high seismic hazard exists in the SE Xianshuihe fault, with a possible Mw6.5-7.3 earthquake risk near Kangding city, confirming predictions from the numerous geophysical studies.

Acknowledgements

This work was financially supported by the National Natural Science Foundation of China [NSFC 42020104007, 41672210, 41941016-03, 41911530773], the China Geological Survey [DD20190059], the Basic Outlay of Scientific Research Work from the Institute of Geology, CAGS [JYYWF20182104], and the Key Special Project for Introduced Talents Team of Southern Marine Science and Engineering Guangdong Laboratory (Guangzhou) (GML2019ZD0201). All geochronology data are in the table and can be downloaded online (at https://zenodo.org/record/4417417#.X_O00C8RqqA).

References

Allen, C. R., Luo, Z., Qian H., Wen X., Zhou H., & Huang, W. (1991). Field study of a highly active fault zone: The XSF of southwestern China. *Geological Society of America Bulletin, 103*, 1178–1199. https://doi.org/10.1130/0016-7606(1991)103<1178:FSOAHA>2.3.CO;2

Bai, M., Chevalier, M. L., Pan, J., Replumaz, A., Leloup, P. H., Métois, M., & Li, H. (2018). Southeastward increase of the late Quaternary slip-rate of the Xianshuihe fault, eastern Tibet. Geodynamic and seismic hazard implications. *Earth and Planetary Science Letters, 485*, 19-31. https://doi.org/10.1016/j.epsl.2017.12.045

Balco, G., Stone, J. O., Lifton, N. A., & Dunai, T. J. (2008). A complete and easily accessible means of calculating surface exposure ages or erosion rates from ^{10}Be and ^{26}Al measurements. *Quaternary Geochronology, 3*, 174-195. https://doi.org/10.1016/j.quageo.2007.12.001

Bevington, P. R., & Robinson, D. K. (2002). Data reduction and error analysis for the physical sciences. 336pp, McGraw-Hill.

Chen, W., Tan, Q., Wen, P., & Liang, X. (1985). Geological map of Kangding (H-47-18). Sichuan

Institute of Geology and Mineral Resources, Scale 1/200,000.

Chen, G., Xu, X., Wen, X., & Wang, Y. (2008). Kinematical transformation and slip partitioning of northern to eastern active boundary belt of Sichuan-Yunnan block. *Seismology and Geology, 30*, 58-85 (in Chinese).

Chen, G., Xu, X., Wen, X., & Chen, Y. (2016). Late Quaternary slip-rates and slip-partitioning on the southeastern Xianshuihe fault system, Eastern Tibetan Plateau. *Acta Geologica Sinica, 90*, 537-554. https://doi.org/10.1111/1755-6724.12689

Cheng, J., Liu, J., Gan, W., Yu, H., & Li, G. (2011). Characteristics of strong earthquake evolution around the eastern boundary faults of the Sichuan-Yunnan rhombic block. *Science China–Earth Sciences, 54*, 1716–1729. https://doi.org/10.1007/s11430-011-4290-2

Chevalier, M. L., Ryerson, F. J., Tapponnier, P., Finkel, R., Van der Woerd, J., Li, H., & Liu, Q. (2005). Slip-rate measurements on the Karakorum fault may imply secular variations in fault motion. *Science, 307(5708)*, 411–414. DOI: 10.1126/science.1105466

Chevalier, M. L., Hilley, G., Tapponnier, P., Van Der Woerd, J., Liu-Zeng, J., Finkel, R. C., Ryerson, F. J., Li, H., & Liu, X. (2011). Constraints on the late Quaternary glaciations in Tibet from cosmogenic exposure ages of moraine surfaces. *Quaternary Science Reviews, 30*, 528–554. https://doi.org/10.1016/j.quascirev.2010.11.005

Chevalier, M. L., Leloup, P. H., Replumaz, A., Pan, J., Metois, M., & Li, H. (2017). Temporally constant slip-rate along the Ganzi fault, NW Xianshuihe fault system, eastern Tibet. *Geological Society of America Bulletin, 130(3/4),* 396–410. https://doi.org/10.1130/B31691.1

Chevalier, M. L., & Replumaz, A. (2019). Bimodal climatic signal for glaciations in SE Tibet: Marine Isotope Stages 2 and 6. *Earth and Planetary Science Letters, 507*, 105-118. https://doi.org/10.1016/j.epsl.2018.11.033

CEA: China Earthquake Administration, Earthquake Disaster Prevention Department. Catalogue of strong earthquakes in Chinese history. Beijing Seismological Press, 1995.

Dai, F. C, Lee, C. F., Deng, J. H., & Tham, L. G. (2005). The 1786 earthquake-triggered landslide

603 dam and subsequent dam-break flood on the Dadu River, southwestern China.
604 *Geomorphology, 65,* 205–221. https://doi.org/10.1016/j.geomorph.2005.06.011
605 Deng, Q., Zhang, P., Ran, Y., Yang, X., Min, W., & Chu, Q. (2003). Basic characteristics of active
606 tectonics of China. *Science in China, 46*, 356–372. https://doi.org/10.1360/03yd9032
607 Friedrich, A. M., Wernicke, B. P., Niemi, N. A., Bennett, R. A., & Davis, J. L. (2003). Comparison
608 of geodetic and geologic data from the Wasatch region, Utah, and implications for the spectral
609 character of Earth deformation at periods of 10 to 10 million years. *Journal of Geophysical*
610 *Research, 108(B4)*, 2199. https://doi.org/10.1029/2001JB000682
611 Gan, W., Zhang, P., Shen, Z., Niu, Z., Wang, M., Wan, Y., Zhou, D., & Cheng, J. (2007). Present-
612 day crustal motion within the Tibetan Plateau inferred from GPS measurements. *Journal of*
613 *Geophysical Research, 112*, B08416. https://doi.org/10.1029/2005JB004120
614 Gaudemer, Y., Tapponier, P., Meyer, B., Peltzer, G., Shunmin, G., Zhitai, C., et al. (1995).
615 Partionning of crustal slip between linked, active faults in the eastern Qilian Shan, and
616 evidence for a major seimic gap, the “Tianzhu gap”, on the western Haiyuan fault, Gansu
617 (China). *Geophysical Journal International, 120*, 599–645.
618 Gorum, T., Fan, X., van Westen, C. J., Huang, R. Q., Xu, Q., Tang, C., & Wang, G. (2011).
619 Distribution pattern of earthquake-induced landslides triggered by the 12 May 2008 Wenchuan
620 earthquake. *Geomorphology, 133*, 152-167. https://doi.org/10.1016/j.geomorph.2010.12.030
621 Gosse, J., & Phillips, F. (2001). Terrestrial in situ cosmogenic nuclides: Theory and application.
622 *Quaternary Science Reviews, 20,* 475–1560. https://doi.org/10.1016/S0277-3791(00)00171-2
623 Hallet, B., & Putkonen, J. (1994). Surface dating of dynamic landforms: young boulders on aging
624 moraines. *Science, 265*, 937-940. DOI: 10.1126/science.265.5174.937
625 He, J., Lu, S., & Wang, X. (2009). Mechanical relation between crustal rheology, effective fault
626 frition, and strike-slip distribution among the Xiaojiang fault system, southeastern Tibet.
627 *Journal of Asian Earth Sciences, 34,* 363–375. DOI: 10.1016/j.jseaes.2008.06.003
628 Heyman, J., Stroeven, A. P., Harbor, J., & Caffee, M. W. (2011). Too young or too old: Evaluating

cosmogenic exposure dating based on an analysis of compiled boulder exposure ages. *Earth and Planetary Science Letters, 302,* 71–80. https://doi.org/10.1016/j.epsl.2010.11.040

Heyman, J. (2014). Paleoglaciation of the Tibetan Plateau and surrounding mountains based on exposure ages and ELA depression estimates. *Quaternary Science Reviews, 91,* 30–41. https://doi.org/10.1016/j.quascirev.2014.03.018

Ji, L., Zhang, W., Liu, C., Zhu, L., Xu, J., & Xu, X. (2020). Characterizing interseismic deformation of the Xianshuihe fault, eastern Tibetan Plateau, using Sentinel-1 SAR images. *Advances in Space Research, 66,* 378–394. https://doi.org/10.1016/j.asr.2020.03.043

Jiang, G., Wen, Y., Liu, Y., Xu, X., Fang, L., Chen, G., Meng, G., & Xu, C. (2015a). Joint analysis of the 2014 Kangding, southwest China, earthquake sequence with seismicity relocation and InSAR inversion. *Geophysical Research Letters, 42,* 3273-3281. https://doi.org/10.1002/2015GL063750

Jiang, G., Xu, X., Chen, G., Liu, Y., Fukahata, Y., Wang, H., Yu, G., Tan, X., & Xu, C. (2015b). Geodetic imaging of potential seismogenic asperities on the Xianshuihe-Anninghe-Zemuhe fault system, southwest China, with a new 3-D viscoelastic interseismic coupling model. *J. Geophys. Res. Solid Earth, 120,* 1855–1873. https://doi.org/10.1002/2014JB011492

Kohl, C. P., & Nishiizumi, K. (1992). Chemical isolation of quartz for measurement of in-situ -produced cosmogenic nuclides. *Geochimica et Cosmochimica Acta, 56,* 3583-3587. https://doi.org/10.1016/0016-7037(92)90401-4

Lal, D. (1991). Cosmic-ray labeling of erosion surfaces-In situ nuclide production rates and erosion models. *Earth and Planetary Science Letters, 104 (2-4),* 424–439. https://doi.org/10.1016/0012-821X(91)90220-C

Li, T., Zhu, Y., Yang, Y., Xu, Y., An, Y., Zhang, Y., Feng, S., Huai, Y., & Yang, J. (2019). The current slip rate of the Xianshuihe fualt zone calculated using mutiple observation data of crustal deformation. *Chinese J. Geophys, 62(4),* 1323-1335 (in Chinese).

Li J., Zhou, B., Li, T., Yang, Y., & Li, Z. (2020). Locking depth, slip rate, and seismicity distribution

along the Daofu–Kangding segment of the Xianshuihe fault system, eastern Tibetan Plateau. *Journal of Asian Earth Sciences, 193,* 104328. https://doi.org/10.1016/j.jseaes.2020.104328

Liang, M. (2019). Characteristics of the Late-Quaternary fault activity of the Xianshuihe Fault. PhD thesis, Institute of Geology, China Earthquake Administration, Beijing.

Liang, M., Chen, L., Ran, Y., Li, Y., Wang, D., Gao, S., Han, M., & Zeng, D. (2020). Late Quaternary activity of the Yalahe fault of the Xianshuihe fault zone, eastern margin of the Tibet Plateau. *Seismology and Geology, 42(2),* 513-525. doi:10.3969/j.issn.0253-4967.2020.02.016 (in Chinese).

Lifton, N., Sato, T., & Dunai, T. J. (2014). Scaling in situ cosmogenic nuclide production rates using analytical approximations to atmospheric cosmic-ray fluxes. *Earth and Planetary Science Letters, 386,* 149-160. https://doi.org/10.1016/j.epsl.2013.10.052

Lisiecki, L.E., & Raymo, M.E. (2005). A Pliocene–Pleistocene stack of 57 globally distributed benthic δ18O records. *Paleoceanography, 20,* PA1003. https://doi.org/10.1029/2004PA001071

Liu, Z., Zhang, G., Hu, Y., & Yang, Y. (1977). Geological map of Gongga (H-47-24). Sichuan Institute of Geology, Scale 1/200,000.

Lu, Y., Shi, R., Hu, Y., & Zhang, S. (1975). Geological map of Yingjing (H-48-19). Sichuan Institute of Geology, Scale 1/200,000.

Mériaux, A. S., Van der Woerd, J., Tapponnier, P., Ryerson, F. J., Finkel, R. C., Lasserre, C., & Xu, X. (2012). The Pingding segment of the Altyn Tagh Fault (91°E): Holocene slip-rate determination from cosmogenic radionuclide dating of offset fluvial terraces. *Journal of Geophysical Research, 117,* B09406. http://dx.doi.org/10.1029/2012JB009289.

Molnar, P., & Tapponnier P. (1975). Cenozoic tectonics of Asia: Effects of a continental collision. *Science, 189(4201),* 4l9-425. https://www.jstor.org/stable/1740465

NSPRC (National Standard of the People's Republic of China). (2016). Seismic ground motion parameter zonation map of China (GB18306-2015).

680 Pan, J., Li, H., Chevalier, M. L., Bai, M., Liu, F., Liu, D., Zheng, Y., Lu, H., & Zhao, Z. (2020). A
681 newly discovered active fault on the Selaha-Kangding segment along the SE Xianshuihe fault:
682 the South Mugecuo fault. *Acta Geologica Sinica, 94(11)*, 3178-3188(in Chinese). doi:
683 10.19762/j.cnki.dizhixuebao.2020196.
684 Papadimitriou, E., Wen, X., Karakostas, V., & Jin, X. (2004). Earthquake Triggering along the
685 Xianshuihe Fault Zone of Western Sichuan, China. *Pure applied Geophysics, 161,* 1683–1707.
686 https://doi.org/10.1007/s00024-003-2471-4
687 Parsons, T., Ji, C., & Kirby, E. (2008). Stress changes from the 2008 Wenchuan earthquake and
688 increased hazard in the Sichuan basin. *Nature, 454,* 509–510.
689 https://doi.org/10.1038/nature07177.
690 Putkonen, J., & Swanson, T. (2003). Accuracy of cosmogenic ages for moraines. *Quaternary*
691 *Research, 59,* 255–261. https://doi.org/10.1016/S0033-5894(03)00006-1
692 Roger, F., Calassou, S., Lancelot, J., Malavieille, J., Mattauer, M., Xu, Z., Hao. Z., & Hou, L.
693 (1995). Miocene emplacement and deformation of the Konga Shan granite (Xianshui He fault
694 zone, west Sichuan, China): Geodynamic implications. *Earth and Planetary Science Letters,*
695 *130,* 201–216. https://doi.org/10.1016/0012-821X(94)00252-T
696 Shao, Z., Xu, J., Ma, H., & Zhang, L. (2016). Coulomb stress evolution over the past 200 years and
697 seismic hazard along the Xianshuihe fault zone of Sichuan, China. *Tectonophysics, 670,* 48-65.
698 https://doi.org/10.1016/j.tecto.2015.12.018
699 Shan, B., Xiong, X., Zheng, Y., Jin, B., Liu, C., Xie, Z., & Hsu, H. (2013). Stress changes on major
700 faults caused by 2013 Lushan earthquake and its relationship with 2008 Wenchuan earthquake.
701 *Sci. China Earth Sci, 56,* 1169-1176. https://doi.org/10.1007/s11430-013-4642-1
702 Shen, Z., Lu, J., Wang, M., & Burgmann, R. (2005). Contemporary crustal deformation around the
703 southeast borderland of the Tibetan Plateau. *Journal of Geophysical Research, 110,* B11409.
704 https://doi.org/10.1029/2004JB003421
705 Stone, J. O. (2000). Air pressure and cosmogenic isotope production. *Journal of Geophysical*

706 *Research, 105(B10)*, 23,753–23,759. https://doi.org/10.1029/2000JB900181
707 Tapponnier, P., & Molnar, P. (1977). Active faulting and Cenozoic tectonics of China. *Journal of*
708 *Geophysical Research, 82,* 2905-2930. https://doi.org/10.1029/JB082i020p02905
709 Tapponnier, P., Xu, Z., Roger, F., Meyer, B., Arnaud, N., Wittlinger, G., & Yang, J. (2001). Oblique
710 stepwise rise and growth of the Tibet plateau. *Science, 294,* 1671–1677. DOI:
711 10.1126/science.105978
712 Toda, S., Lin, J., Meghraoui, M., & Stein, R. S. (2008). 12 May 2008 M = 7.9 Wenchuan, China,
713 earthquake calculated to increase failure stress and seismicity rate on three major fault systems.
714 Geophysical Research Letters, 35, L17305. https://doi.org/10.1029/2008GL034903
715 Wang, E., Burchfiel, B. C., Royden, L. H. Chen, L., Chen, J., Li, W., & Chen, Z. (1998). The
716 Cenozoic Xianshuihe– Xiaojiang, Red River, and Dali fault systems of southwestern Sichuan
717 and central Yunnan, China. *Geological Society of America Special Paper, 327,* 108p.
718 https://doi.org/10.1130/SPE327
719 Wang, E., & Burchfiel, B.C. (2000). Late Cenozoic to Holocene deformation in southwestern
720 Sichuan and adjacent Yunnan, China, and its role in formation of the southeastern part of the
721 Tibetan Plateau. *Geological Society of America Bulletin, 112*, 413–423.
722 https://doi.org/10.1130/0016-7606(2000)112<413:LCTHDI>2.0.CO;2
723 Wang, H., Wright, T.J., & Biggs, J. (2009). Interseismic slip rate of the northwestern Xianshuihe
724 fault from InSAR data. *Geophysical Research Letters, 36,* L03302.
725 https://doi.org/10.1029/2008GL036560
726 Wang, S., Jiang, G., Xu, T., Tian, Y., Zheng, D., & Fang, X. (2012). The Jinhe–Qinghe fault—
727 Aninactive branch of the Xianshuihe–Xiaojiang fault zone, Eastern Tibet. *Tectonophysics, 544-*
728 *545*, 93-102. https://doi.org/10.1016/j.tecto.2012.04.004
729 Wang, W., Qiao, X., Yang, S., & Wang, D. (2017). Present-day velocity field and block kinematics
730 of Tibetan Plateau from GPS measurements. *Geophysical Journal International, 208*, 1088-
731 1102. https://doi.org/10.1093/gji/ggw445

732 Wang, Y., Wang, M., & Shen, Z. (2017). Block-like versus distributed crustal deformation around
733 the northeastern Tibetan plateau. *Journal of Asian Earth Sciences, 140*, 31-47.
734 https://doi.org/10.1016/j.jseaes.2017.02.040
735 Wang, W., Qiao, X., & Ding, K. (2020). Present-day kinematics in southeastern Tibet inferred from
736 GPS measurements. *Journal of Geophysical Research, e2020JB021305*.
737 https://doi.org/10.1029/2020JB021305
738 Wang, M., & Shen, Z. (2020). Present-day crustal deformation of continental China derived from
739 GPS and its tectonic implications. *Journal of Geophysical Research, 125,* e2019JB018774.
740 Doi:10.1029/2019JB018774.
741 Wells, D.L., & Coppersmith, K.J. (1994). New empirical relationships among magnitude, rupture
742 length, rupture width, rupture area, and surface displacement. *Bulletin of the Seismological*
743 *Society of America, 84*, 974–1002.
744 Wen, X. (2000). Character of rupture segment of Xianshuihe- Zemuhe–Anninghe fault zone,
745 western Sichuan. Seismology and Geology, 22, 239–249.
746 Wen, X., Ma, S., Xu, X., & He, Y. (2008). Historical pattern and behavior of earthquake ruptures
747 along the eastern boundary of the Sichuan–Yunnan faulted-block, southwestern China. *Physics*
748 *of the Earth and Planetary Interiors, 168 (1–2)*, 16–36.
749 https://doi.org/10.1016/j.pepi.2008.04.013
750 Xie, Z., Zheng, Y., Liu, C., Shan, B., Riaz, M. S., & Xiong, X. (2017). An integrated analysis of
751 source parameters, seismogenic structure, and seismic hazards related to the 2014 M S 6.3
752 Kangding earthquake, China. *Tectonophysics, 712,* 1-9.
753 https://doi.org/10.1016/j.tecto.2017.04.030
754 Xu, K. Liu, J., Liu, X., Liu, J., & Zhao, F. (2020). Multiscale crustal deformation around the
755 southeastern margin of the Tibetan Plateau from GNSS observations. *Geophysical Journal*
756 *International, 223,* 1188–1209. https://doi.org/10.1093/gji/ggaa289
757 Yan, B., & Lin, A. (2015). Systematic deflection and offset of the Yangtze River drainage system

along the strike-slip Ganzi-Yushu-Xianshuihe Fault Zone, Tibetan Plateau. *Journal of Geodynamics, 87,* 13-25. https://doi.org/10.1016/j.jog.2015.03.002

Yan, B., & Lin, A. (2017). Holocene Activity and Paleoseismicity of the Selaha Fault, Southeastern Segment of the Strike-Slip Xianshuihe Fault Zone, Tibetan Plateau. *Tectonophysics, 694(2),* 302–318. https://doi.org/10.1016/j.tecto.2016.11.014

Yan, B., Jia, D., & Lin, A. (2018). Late Pleistocene-Holocene tectonic landforms developed along the strikeslip Xianshuihe Fault Zone, Tibetan Plateau, China. *Journal of Geodynamics, 120,* 11–22. https://doi.org/10.1016/j.jog.2018.05.005

Yan, B., Wang, M., Jia, D., & Cui, J. (2019). Investigation and magnitude re-evaluation of the 1955 Zheduotang earthquake, eastern Tibetan Plateau, China. *Geological Journal, 2019,* 1–13. https://doi.org/10.1002/gj.3628

Yang, W., Cheng, J., Liu, J., & Zhang, X. (2015). The Kangding earthquake swarm of November, 2014. *Earthquake Science, 28(3),* 197-207. https://doi.org/10.1007/s11589-015-0123-2

Zechar, J. D., & Frankel, K. L. (2009). Incorporating and reporting uncertainties in fault slip rates. *Journal of Geophysical Research, 114,* B12407. https://doi.org/10.1029/2009JB006325

Zhang, P.Z. (2013). A review on active tectonics and deep crustal processes of the Western Sichuan region, eastern margin of the Tibetan Plateau. *Tectonophysics, 584,* 7-22. https://doi.org/10.1016/j.tecto.2012.02.021

Zhang, Y., Yao, X., Yu, K., Du, G., & Guo, C. (2016). Late Quaternary slip-rate and seismic activity of the Xianshuihe fault zone in southwest China. *Acta Geologica Sinica, 90,* 525-536. https://doi.org/10.1111/1755-6724.12688

Zhang, Y., Replumaz, A., Leloup, P. H., Wang, G., Bernet, M., van der Beek, P., Paquette, J. L., Chevalier, M. L. (2017). Cooling history of the Gongga batholith: implications for the Xianshuihe Fault and Miocene kinematics of SE Tibet. *Earth and Planetary Science Letters, 465,* 1-15. https://doi.org/10.1016/j.epsl.2017.02.025

Zheng, G., Wang, H., Wright, Tim J., Lou, Y., Zhang, R., Zhang, W., Shi, C., Huang, J., & Wei, N.

(2017). Crustal deformation in the India-Eurasia collision Zong from 25 years of GPS measurements. *Journal of Geophysical Research, 122*, 9290–9312. https://doi.org/10.1002/2017JB014465

Zhou, R., He, Y., Huang, Z., Li, X., & Yang, Z. (2001). The slip rate and recurrence of strong earthquakes of Qianning-Kangding segment, the Xianshuihe fault zone. *Acta Seismologica Sinica, 23(3)*, 250-261 (in Chinese).